UC Berkeley
UC Berkeley Previously Published Works

Title

Two Brain Pathways Initiate Distinct Forward Walking Programs in Drosophila

Permalink

Journal

ISSN

Authors

Bidaye, Salil S
Laturney, Meghan
Chang, Amy K
et al.

Publication Date

DOI

Peer reviewed

Two brain pathways initiate distinct forward walking programs in *Drosophila*

Salil S. Bidaye[1,*], **Meghan Laturney**[1], **Amy K. Chang**[1], **Yuejiang Liu**[1], **Till Bockemühl**[2], **Ansgar Büschges**[2], **Kristin Scott**[1,3,*]

[1]Department of Molecular and Cell Biology and Helen Wills Neuroscience Institute University of California, Berkeley Berkeley, CA 94720

[2]Department of Animal Physiology, Institute of Zoology, University of Cologne, 50674 Cologne, Germany

Summary

An animal at rest or engaged in stationary behaviors can instantaneously initiate goal-directed walking. How descending brain inputs trigger rapid transitions from a non-walking state to an appropriate walking state is unclear. Here, we identify two neuronal types, P9 and BPN, in the *Drosophila* brain that, upon activation, initiate and maintain two distinct coordinated walking patterns. P9 drives forward walking with ipsilateral turning, receives inputs from central courtship-promoting neurons and visual projection neurons and is necessary for a male to pursue a female during courtship. In contrast, BPN drives straight, forward walking and is not required during courtship. BPN is instead recruited during and required for fast, straight, forward walking bouts. Thus, this study reveals separate brain pathways for object-directed walking and fast, straight, forward walking, providing insight into how the brain initiates context-appropriate walking programs.

eTOC Blurb:

Bidaye et al. characterize two neuronal types P9 and BPN that drive two distinct forward walking programs in *Drosophila.* These brain pathways recruit the downstream motor circuits for walking in a task-specific manner such that a stationary animal can directly switch into a specific walking mode.

Graphical Abstract

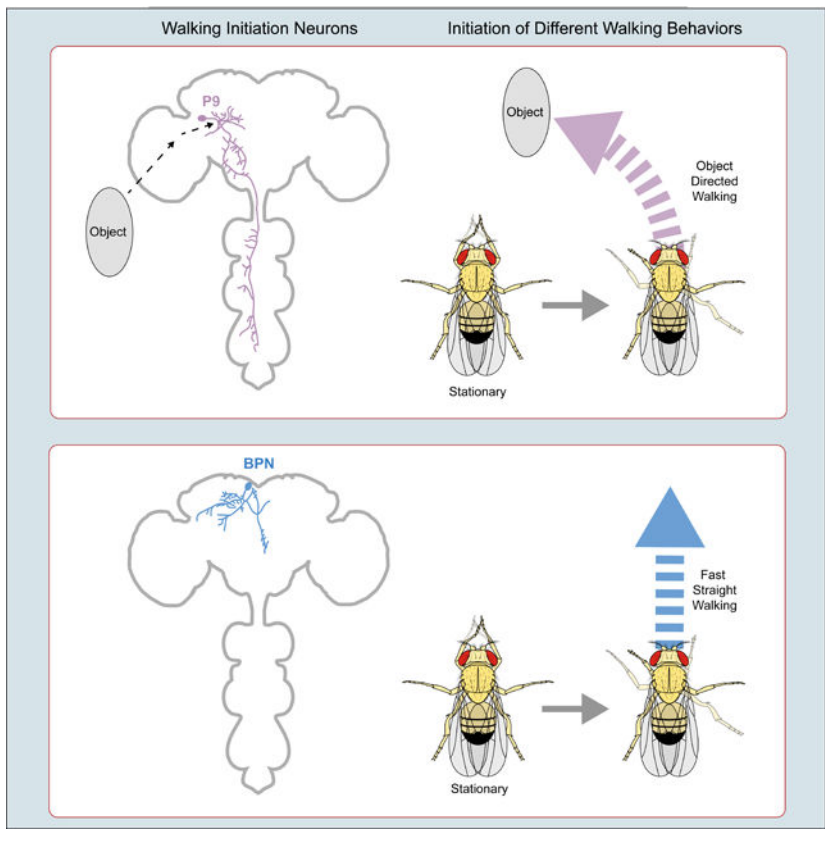*Correspondence: salilbidaye@berkeley.edu, kscott@berkeley.edu.

[3]Lead Contact

Declaration of Interests

The authors declare no competing interests.

Introduction

Animals show a remarkable ability to seamlessly adjust their walking patterns in response to dynamic sensory stimuli, as they navigate an unpredictable environment. Moreover, animals not only can modify an ongoing walking pattern, but also have the ability to transition from a non-walking state directly into a goal-appropriate walking state. For example, an animal may suddenly spring into an escape run at the sight of a predator or initiate a spontaneous exploratory walking bout. However, it is unclear how the nervous system generates rapid, task-appropriate locomotion.

In both vertebrates and invertebrates, the leg movements that comprise a walking pattern are hypothesized to be controlled by a distributed network of pattern generating modules in the spinal cord or nerve cord, with each module controlling the movement of each leg joint (Brown, 1911; Büschges et al., 1995; Cheng et al., 1998; Grillner and Zangger, 1975; Hägglund et al., 2013; Ryckebusch and Laurent, 1993). Sensory feedback as well as central neural circuits are crucial for coordinating this network in order to generate walking (Bässler and Büschges, 1998; Shik and Orlovsky, 1976; Tuthill and Azim, 2018). These leg movement control circuits exist in a fundamentally different functional state in a non-walking animal versus a walking animal. For example, classical studies show that the same force applied to the leg of a non-moving animal produces a distinct motor output compared to that of an animal producing voluntary leg movements (Bässler, 1976; Pearson, 1995). Similarly, inter-leg coordination during stationary behaviors like grooming

(Mueller et al., 2019) or searching (Berg et al., 2015) is completely different from that during walking (Wosnitza et al., 2013, Mendes et al., 2013). Despite these distinct functional states, descending inputs from the brain are able to instantaneously switch the spinal cord or nerve cord circuits from a non-walking state into a walking state (Bidaye et al., 2018; Jordan et al., 2008; Ruder and Arber, 2019). Whether walking is initiated by concerted population activity of descending inputs that coordinate pattern generating modules in the spinal cord or whether a single brain command can drive such a complex state change is unknown. Furthermore, it is unclear whether walking initiated in different contexts, such as escaping, pursuing, or exploring, results from distinct descending inputs or from modulation of a common descending pathway for walking initiation. To distinguish potential brain mechanisms for locomotor control and the generation of context-dependent behavior, it is essential to elucidate descending pathways that encode walking initiation.

In mammals, brainstem circuits are critical for walking initiation. The mesencephalic locomotor region (MLR) is one such brainstem region implicated in walking initiation across different mammalian species (Shik and Orlovsky, 1976; Skinner and Garcia-Rill, 1984). The MLR activates neurons in the reticular formation in the hindbrain that in turn drive spinal cord networks for locomotion. Recent studies have begun delineating mouse MLR and brainstem regions into molecularly defined subsets that control specific aspects of locomotion (Bouvier et al., 2015; Caggiano et al., 2018; Capelli et al., 2017). However, given the heterogeneity of these brain areas in terms of functions, cell-types, and projection targets, it remains challenging to examine how descending pathways recruit spinal cord circuits for walking initiation.

In insects, the small number of ~300–500 descending neurons (DNs) that project to the ventral nerve cord (VNC) provides the opportunity to finely probe how locomotor control is encoded in descending pathways. Although specific DNs have been associated with specific aspects of walking including walking initiation in different insect species (Ache et al., 2015; Böhm and Schildberger, 1992; Burdohan and Comer, 1996; Zorović and Hedwig, 2013), lack of reproducible access to these neurons makes it difficult to examine their function. In addition, little is known about how higher brain neurons control context-specific walking initiation in insects. The sophisticated genetic tools in *Drosophila melanogaster* allow reproducible access to specific neurons including DNs (Namiki et al., 2018) and greatly facilitate functional characterization. Recent work revealed that many DNs can modify an ongoing walking program (Bidaye et al., 2014; Cande et al., 2018). In addition, the activity of a few DNs has been shown to correlate with locomotor patterns (Chen et al., 2018; Tschida and Bhandawat, 2015). However, it is still unclear if specific brain inputs, both at the level of DNs as well as higher brain areas, can initiate a coordinated walking pattern and how distinct walking initiations are manifested in different behavioral contexts.

Here, we leveraged recently developed genetic tools and coupled them with novel behavioral assays and functional imaging to examine walking initiation neurons in *Drosophila*. From a targeted optogenetic screen for walking initiation neurons, we identified two neuronal types that initiate two distinct modes of forward walking: P9 DN induces forward walking with an ipsilateral turning component, whereas novel higher brain neurons, which we name Bolt protocerebral neurons (BPN), induce straight forward walking. Functional connectivity and

neural silencing studies revealed that the ipsilateral turning walking program driven by P9 contributes to object directed walking in the context of courtship. In contrast, BPNs were dispensable for courtship. Instead, *in-vivo* imaging and behavioral experiments showed that BPNs are specifically necessary for fast, long duration, straight forward walking. These studies show that the activity of specific brain neurons is sufficient to switch downstream motor control circuits from a non-walking state into a walking state and provide evidence for distinct descending pathways for walking initiations in different contexts.

Results

A neural activation screen identifies candidate walking initiation neurons

To examine how animals initiate walking rather than modify an ongoing walking pattern, we designed an optogenetics based assay to screen for neurons that trigger walking in non-walking flies. Flies spend most of their time walking when restricted to a small arena where they cannot fly. To bias flies toward a non-walking state, flies were dusted with fine powder to induce grooming (Seeds et al., 2014). This greatly reduced baseline walking activity, an essential condition to screen for walking initiation.

DNs send information from the brain to the VNC and represent a critical relay for motor control. We therefore screened 156 lines that targeted potential DNs, consisting of the DN split-Gal4 collection which covers over a third of all *Drosophila* DNs, (Namiki et al., 2018) as well as selected Gal4 lines from the Janelia and VT collections that label DNs (Bidaye et al., 2014; Jenett et al., 2012; Tirian and Dickson, 2017). Powdered and non-powdered flies expressing the red-shifted channelrhodopsin CsChrimson (Klapoetke et al., 2014) in neural candidates were stimulated with light and locomotion of single flies was monitored (Figure 1A). Three lines increased walking more than 5 fold relative to controls when covered with powder and more than 1.2 fold when not powdered (Figures 1B and S1A). Upon retest with acute stimulation, two of the lines, *SS01540* and *SS01587* from the DN split-Gal4 collection (Namiki et al., 2018), reliably initiated walking in powdered flies (Figures 1C, S1B and Video S1).

If neurons in these lines are bona fide walking initiation neurons, then neural activation should lead to walking in a context other than grooming. Copulation is a persistent non-walking state in which the male and the female remain stationary for extended periods (Crickmore and Vosshall, 2013), although the female posture is compatible with walking. We therefore expressed CsChrimson in *SS01540* and *SS01587* and transiently activated the neurons of females mid-copulation. Remarkably, the females reliably initiated walking while remaining conjoined with the mounted male (Figures 1D, S1C and Video S2). This demonstrates that activation of specific neurons in the fly initiates walking and overrides competing behavioral states, including grooming and copulating.

Although both lines induced forward walking, *SS01540* and *SS01587* induced forward walks with different trajectories (Figures 1E, 1F, S1, and Video S1). *SS01540* activation elicited forward walking with a strong turning component whereas *SS01587* activation induced straight forward walking, as indicated by rotation, angular velocity, and straightness measures, for both grooming and copulation assays (Figures 1E, 1F, S1D–G). Thus, via

a targeted optogenetic screen, we identified two walking initiation candidates that induce two modes of forward walking, suggesting that they might represent activation of distinct walking initiation pathways.

P9 DNs initiate forward walking with an ipsilateral turning component

To begin to examine neural pathways that initiate forward walking, we focused on *SS01540* as its expression pattern is sparse. This line labels DNp09 (henceforth referred to as P9) (Namiki et al., 2018), a pair of ipsilateral DNs (one cell per hemisphere) and a few additional neurons (Figures S2A and S2B). We generated a second P9 split-Gal4 line (P9S2) that targets P9 but does not share off-target cells with *SS01540* (Figures S2C and S2D). Activating P9S2 neurons induced a walking initiation phenotype with a strong turning component similar to *SS01540* (Figure S2E), confirming the role of P9 in walking initiation.

Although walking initiation was previously never explicitly examined, *SS01540* neural activation has been reported to induce a transient increase in locomotion followed by stopping/freezing (Cande et al., 2018; Zacarias et al., 2018). However, after testing four different genetic driver and reporter combinations, we found that freezing was observed in only one genotype, although all genotypes strongly label P9 and initiate walking on neural activation (Figures S2A–D and S2F). Whether the freezing phenotype is a consequence of relatively high CsChrimson expression in P9 or off-target neurons labeled by this genotype (Figure S2G) is unclear. Regardless, in all cases, optogenetic stimulation increased both forward and angular velocity, corroborating that P9 activation elicits walking with a turning component. Although the above results were obtained in female flies, activation of P9 in male flies showed similar walking initiation phenotypes (Figure S2H, I).

P9 dendrites are in the posterior protocerebrum and send presynaptic outputs in the subesophageal zone (SEZ) and the ipsilateral leg VNC neuropils (Figures 2A and 2B). The ipsilateral dendrites and axons suggest that activation of a single P9 neuron might lead to turning in a specific direction. Indeed, mosaic animals with CsChrimson stochastically expressed in both P9 neurons initiated walking with turns in both directions on activation (Figure 2C), whereas all animals that expressed CsChrimson unilaterally in the right P9 initiated forward walking with rightward turns (Figure 2D) and in the left P9 initiated leftward turns (Figure 2E) upon neural activation (Video S3). The manipulation of single P9 neurons demonstrates that P9 is the causal neuron in the split-Gal4 *(SS01540)* line that initiates a complex locomotor program of forward walking with ipsilateral turns. Moreover, these studies reveal that unilateral activation of a single P9 neuron initiates ipsilateral forward turns and raise the possibility that P9 activity may be recruited to initiate walking towards an ipsilateral attractive stimulus.

P9 neurons receive inputs from courtship promoting neurons and visual projection neurons

As P9 directly links the central brain with the VNC and initiates ipsilateral forward turns, we hypothesized that P9 might be a key relay in a sensorimotor pathway involved in steering toward attractive objects. One vital behavior requiring a fly to frequently turn toward an attractive stimulus is male pursuit of a female during courtship behavior (Agrawal and

Dickinson, 2019; Agrawal et al., 2014; Dickson, 2008; Kohatsu and Yamamoto, 2015). Consistent with the hypothesis that P9 might participate in visually guided pursuit as seen during courtship, P9 dendrites arborize in close proximity to pC1, the master courtship promoting neurons in the fly (Bath et al., 2014; Hoopfer et al., 2015; Inagaki et al., 2014; Koganezawa et al., 2016; Kohatsu et al., 2011a; von Philipsborn et al., 2011) and lobular columnar (LC) neurons that encode visual features relevant for specific behaviors (Figures 3 A and S3A, B).

To test if P9 receives excitatory functional inputs from pC1 (Koganezawa et al., 2016) or five LC neural classes implicated in object tracking, courtship or figure detection (Kele and Frye, 2017; Kohatsu et al., 2011b; Ribeiro et al., 2018; McKinney and Ben-Shahar, 2018; Aptekar et al., 2015), we monitored responses in P9 by GCaMP6s calcium imaging while optogenetically activating upstream candidates with Chrimson. pC1 or LC9 activation produced reliable calcium transients in P9 (Figures 3B and 3C). The other tested LC split-Gal4 drivers did not elicit P9 responses (Figure 3C). Stronger activation of LC11 with a sparse LC11-Gal4 also elicited reliable P9 responses (Figure 3C) indicating that LC11 is a potential P9 input.

To examine whether P9 is directly synaptically coupled to any of these functionally upstream neurons, we searched the newly available *Drosophila* central brain connectome generated by EM reconstruction (Meissner et al., 2020). The VPNs and pC1 neuronal classes are annotated in the dataset. Although P9 was not annotated, we were able to identify and verify P9 (STAR Methods). While P9 receives inputs from multiple neurons including VPNs, the highest number of inputs come from LC9 neuronal class. There are 1–13 synapses per LC9 cell, totaling 265 synapses from the LC9 class onto a single P9 cell (Figure 3D, E). In addition, LC11 and P9 are connected via an intermediate neuron (cell ID 1385093648, Figures 3E and S3C), consistent with the functional connectivity studies and the lack of direct anatomical overlap by light microscopy. There is also direct input (2 synapses) from pC1d to P9 (Figure 3D, E) as well as several indirect contacts between pC1d and P9 via intermediate neurons with stronger connections (>5 synapses; one strong indirect connection (ADM01od), is shown in Figures 3E and S3D). It should be noted that although P9 shows identical anatomy and behavioral phenotypes in males and females (males: Figure S2H,I, females: Figure 2, S2A–E), pC1 is a sexually dimorphic neural class; females have 5 pC1 cells denoted as pC1a-e, whereas males have at least 60 pC1 neurons (Ren et al., 2016). As the EM connectivity data is derived from a female brain and the functional connectivity studies were done with male brains, it remains possible that there are more direct pC1-P9 connections in male brains.

Overall, these functional and anatomical connectivity studies demonstrate that P9 receives excitatory inputs from pC1 and LC neurons that participate in object detection and/or tracking. This suggests that P9 might function as a node for integration of courtship state and visual features to drive visually guided pursuit during courtship (Figure 3F).

P9 neurons are essential for object directed walking during courtship

To directly test the hypothesis that P9 participates in orienting a male toward a female during courtship, we blocked the synaptic output of P9 by selective expression of tetanus

toxin (TeTx) in males and examined male courtship behavior. P9 silenced males showed overt courtship defects, with only a fraction of flies successfully copulating in a 10-minute assay (Figures 4A and 4B). Blocking transmission of potential P9 inputs, pC1 and LC9, also significantly reduced copulation (Figures 4B and S3E). To examine whether P9 silenced males show defects in following females, we evaluated the female's position with respect to the male and the time spent in close proximity to the male pre-copulation (Figures 4C and 4D). This revealed that P9 silenced males showed significant defects in pursuing females. Silencing LC9 also decreased following, while silencing other candidate upstream neurons had no significant effect (Figure 4D).

Most control flies copulated soon after the assay started and showed short mate pursuit sequences, making it challenging to evaluate the tracking ability. To encourage the male to perform long and complex tracking behavior, we replaced the target female with a virgin female expressing CsChrimson in P9 neurons. The "remote-controlled" female was intermittently triggered to perform sudden forward walking and turning via P9 activation throughout the assay, making it a challenging target. Control males engaged in long following sequences chasing remote-controlled females (Figures 4E, 4F and Video S4). Moreover, control males exhibited rapid velocity changes that were synchronized with the artificially evoked sudden velocity changes of the remote-controlled females (Figures 4G, 4H and Video S4). P9 silenced males showed significantly reduced following of the remote-controlled females (Figures 4E and 4F). Blocking activity of neurons functionally upstream of P9, including LC9 and pC1, also resulted in courtship following deficits (Figures 4F and S3F). In addition, the velocities of P9 silenced males showed little correlation to the velocities of the remote-controlled females (Figures 4G and 4H), although the males walked at similar average velocities as controls (Figure S3G). To test male pursuit towards non-manipulated females while still encouraging long and complex following behavior, we designed flat, low ceiling arenas, which enhanced the repertoire of female locomotion. Results in this assay were similar to the remote-controlled female assay (Figures S3H–J), demonstrating that P9 and upstream neurons are required for following a female during courtship.

Although the average walking velocities of P9 silenced flies were similar to controls, we wondered if defects in stepping or inter-leg coordination were responsible for the poor object pursuit of these flies. To test this, we analyzed the walking pattern of P9 silenced flies in fine detail via high speed recordings and deep learning based automated leg position tracking (Mathis et al., 2018). This analysis showed that P9 silenced flies have normal stepping parameters and inter-leg coordination (Figure S4). Thus, the behavioral deficits observed in courtship do not reflect uncoordinated walking.

Taken together, these studies demonstrate a specific role for P9 in visually guided pursuit behavior during courtship. Neurons functionally upstream of P9, including LC9 and pC1, also showed courtship following deficits, supporting the notion that they contribute to an object tracking pathway that is likely gated by courtship state. While P9 inactivation precludes a male's ability to follow a female, other aspects of locomotion are unaffected. Thus, the studies of P9 reveal a specific locomotor program for object-directed walking.

Bolt Protocerebral Neurons (BPNs) initiate straight forward walking

P9 impacts a specific walking program, suggesting that there may be independent pathways for different forward walking behaviors. To examine if there are multiple independent pathways that drive different walking behaviors, we characterized the walking behavior of the second candidate walking initiation line, *SS01587* (Namiki et al., 2018), which induced straight forward walking without turns upon activation (Figures 1E, 1F, S1B–G).

SS01587 labels DN0p28 and 7 other neuronal types (Figure S5A). To determine the neurons in *SS01587* causal for walking initiation, we used mosaic strategies to restrict the number of neurons expressing CsChrimson in *SS01587* and screened for mosaic animals that initiated walking in grooming flies upon transient activation. Comparing CsChrimson expression in the brains of walking and non-walking individuals revealed that activation of a single neuronal type in *SS01587* is correlated with walking initiation (Figure S5B). This neuronal type, which we name Bolt Protocerebral Neurons (BPNs) in homage to sprinter Usain Bolt, is a cluster of ~8 cells per hemisphere, with cell bodies located near the posterior superior margin of the fly brain (Figure S5C). To obtain specific, reproducible genetic access to BPNs, we generated two new split-Gal4 reagents that label BPNs (Figures 5A and S5D). Both lines triggered robust walking initiation in grooming flies upon optogenetic activation (Figures 5B and S5E–H). As with *SS01587,* these flies initiated straight forward walking (Figure S5F).

BPN dendrites arborize extensively in the lateral protocerebrum and axons project along the contralateral midline towards the subesophageal zone (SEZ) (Figure 5C). If BPNs receive inputs regarding spatially localized sensory stimuli, then one prediction would be that unilateral activation of BPNs would produce a turning component to the induced walking, similar to P9 unilateral activation. However, unlike P9, unilateral activation of BPNs did not confer a turning bias and instead evoked straight forward walks. Comparing translational velocity and angular velocity for animals expressing CsChrimson in the left BPNs, right BPNs, or both revealed no differences (Figures 5D–F). Thus, BPN activation produces fast, straight, forward walking without a turning bias.

The activation phenotypes of BPNs and P9 are distinct, with P9 activation eliciting walking with ipsilateral turns, and BPNs eliciting straight walks, suggesting that they are components of two independent walking initiation pathways. Consistent with this, simultaneously activating BPN and P9 increased walking velocities and distance travelled compared to activation of each line alone (Figure S5L) and added a turning component compared to straight walking observed on BPN activation (Figure S5L). Also, silencing BPN did not affect copulation or mate pursuit in all courtship assays (Figure 4 and S3), arguing that BPN is not essential for object directed walking. Additionally, as BPN is a higher brain neuron and P9 is a descending neuron, we tested whether BPN is upstream of P9, by CsChrimson mediated BPN activation and P9 GCaMP6s imaging, and found that BPN did not activate P9 (Figure 3C). Finally, BPN candidate downstream neurons, identified using trans-synaptic labeling (Talay et al, 2017), contained an SEZ neuronal type and descending axonal tracts poised to relay information to motor circuits but did not contain P9 (Figure S5, J–K). Taken together, these studies demonstrate that BPN and P9 participate in independent walking initiation pathways, consistent with their different behavioral phenotypes.

BPN activity correlates with high velocity straight, forward walking

We examined BPN activity during spontaneous walking behavior to evaluate its response properties *in vivo.* BPN activity was monitored by GCaMP6s imaging of BPN soma while flies were walking on an air-supported ball and their locomotion was recorded (Figure 6A). Interestingly, mean BPN activity was strongly correlated to walking velocity only in a subset of walking bouts and trials. Not all BPN soma showed measurable activity; these were not included in analyses (STAR Methods).

To examine when BPNs are recruited by the fly, we mapped BPN calcium activity onto the walking trajectory. In one illustrative example, the walking trajectory was initially comprised of tight turning bouts and low BPN activity uncorrelated to translational velocity (Figures 6B–D). Subsequently, the trajectory was comprised of longer straight walking bouts and high BPN activity correlated to translational velocity (Figure 6E), indicating that BPNs might be specifically recruited during straight walking. Overall, BPN activity was high when translational velocity (V_T) was high and angular velocity (V_A) was low (Figures 6F–H and S6A). Additionally, BPN activity was correlated to duration of walking bouts (T_W) (Figure S6A). A linear regression model using V_T, V_A and T_W as predictors of BPN activity showed positive regression coefficients for V_T and T_W, but negative for V_A (Figure S6B) corroborating that BPNs are preferentially active during straight, long duration walking bouts.

To obtain an unbiased view of how BPN activity correlates with walking, data across 3 flies and 5 imaging sessions (Figure S6C–H), amounting to 589 walking bouts, was pooled for unbiased k-means clustering in a 4D space of [mean BPN activity, V_T, V_A, T_W]. One cluster corresponds to high BPN activity, V_T and T_W, but low V_A (red cluster, Figures 6I and S6H–K). This cluster is comprised of high velocity, long duration, low turning bouts and represents the majority of instances when BPNs were highly active across all flies and imaging sessions (Figures 6J and S6H–K). In contrast, the other two clusters are comprised of low BPN activity and high angular velocity bouts (Figures 6I, 6J and S6H–K). Thus, this independent analysis confirms that BPN activity specifically increases during fast, long, straight walks.

In contrast P9 was not active during spontaneous walking in similar *in vivo* imaging experiments further confirming its role in specific behavioral contexts like courtship (Figure S6 L–N).

BPN activity reciprocally regulates fast, straight, forward walking

If BPN activity drives fast, straight, long duration, forward walking without turns, then one prediction is that artificially scaling BPN activity would proportionally scale walking bout duration and translational velocity but not angular velocity. Indeed, increasing the light stimulation frequencies (from 10–150 Hz) of CsChrimson-mediated BPN activation increased the walking duration and translational velocity but not angular velocity (Figure 7A). Conversely, freely walking flies with synaptic transmission blocked in BPNs showed reduced walking duration and translational velocity (and angular velocity because they walk less) (Figure 7B). Moreover, pooled analysis of control and BPN silenced walking bout data

showed that BPN silenced flies lacked long duration and high translational velocity walking bouts (Figure S7A–C). In addition, control flies initiated high speed walking upon sudden exposure to bright green light, whereas BPN silenced flies showed a smaller velocity change and lower maximum velocities (Figure 7C). Critically, high resolution analyses of leg kinematics in freely walking flies revealed that BPN silenced flies were not uncoordinated (Figure S7D–M) but instead walked slowly as a result of an increased step period, due to an increased stance duration (Figure 7E), resembling the gait of slow walking flies (DeAngelis et al., 2019; Wosnitza et al., 2013). In contrast, P9 silenced flies did not show walking gaits different from controls (Figure S4). Taken together, these experiments demonstrate an essential role for BPNs in driving walking at high translational velocity and further demonstrate that P9 and BPN drive distinct motor programs.

Discussion

This study identifies two classes of central neurons sufficient to initiate coordinated forward walking in the fly, representing a significant step forward in studies of locomotor control. P9 receives inputs from courtship promoting neurons and visual projection neurons and drives forward walking with an ipsilateral turning component. Moreover, P9 is required during object directed walking in the context of courtship, whereas BPN is not required for object directed walking in this context. Instead, BPN activity is correlated with straight, long, fast walking bouts, and manipulating activity of these neurons modifies walking speed and duration without affecting turning. Thus, the characterization of these neurons reveals two distinct pathways that initiate two different forward walking programs in different behavioral contexts.

Distinct walking initiation commands initiate distinct walking programs

P9 and BPN uncover separate brain pathways for object-directed forward steering and fast, straight, forward walking, respectively. The existence of these independent walking initiation pathways argues that specific brain inputs can drive distinct and complete walking programs in a context specific manner. This may be achieved by driving a common downstream walking circuit that is modulated to generate specific walking modes, as suggested by neuromechanical models for directional control of walking (Guschlbauer et al., 2012; Tóth and Daun, 2019; Tóth et al., 2012). Alternatively, these pathways may recruit distinct downstream premotor circuits, each generating a distinct motor pattern. Examining the downstream circuits of these walking initiation pathways will help unravel the mechanisms of these distinct walking initiations.

Complex motor patterns observed in natural behaviors likely result from combined activity of populations of descending commands from the brain (Pearson, 1993). Interactions among DNs may bring about a concerted change in the functional state of nerve cord circuits, as seen in crawling circuits in *C. elegans* (Piggott et al., 2011) and *Drosophila* larvae (Carreira-Rosario et al., 2018). Therefore, in natural behaviors, P9 and BPN pathways may be active in parallel with other descending signals. An interesting question is whether a population of descending commands generates a motor output more complex than the sum of its constituents. Genetic access to characterized walking initiation neurons (P9 and BPN)

will now enable examination of this question and will guide future experiments aimed at elucidating how brain neurons influence walking control.

The P9 walking program provides steering control during object tracking

From an activation screen of approximately half of all DNs in the fly (Namiki et al., 2018), the P9 DNs were the only DNs to initiate walking. These results argue that very few single DNs encode forward walking initiation. Similarly, a previous unbiased behavioral screen revealed MDN as the only DN sufficient to drive backward walking (Bidaye et al., 2014). While DN combinations likely elicit and modulate walking, these studies argue that P9 neurons have a privileged role as a DN class triggering a complete forward walking program.

Previous studies have shown the strong importance of vision in pursuing a potential mate during courtship (Cook, 1980; Kohatsu and Yamamoto, 2015; Markow and Manning, 1980; Ribeiro et al., 2018). Male flies initiate walking towards any object with visual characteristics that grossly match that of a potential mate (Agrawal and Dickinson, 2019), indicating that visual information may directly influence walking control neurons. Here, we showed that P9 receives direct inputs from LC9 that serve as feature detectors, arguing that P9 participates in a shallow pathway from visual detection to motor command. Direct connections between visual projection neurons and DNs are also seen in the Giant Fiber escape pathway (Klapoetke et al., 2017; von Reyn et al., 2017; Strausfeld and Bassemir, 1983) and in visually guided flight control (Strausfeld and Gronenberg, 1990; Suver et al., 2016), suggesting a common circuit motif to minimize response times when rapid action is required.

In addition to visual inputs, P9 is also activated by pC1 neurons, master regulators of courtship behavior that integrate olfactory, pheromonal, and auditory cues and drive a complex courtship sequence (Clowney et al., 2015; Coen et al., 2016; Kallman et al., 2015; Kohatsu and Yamamoto, 2015; von Philipsborn et al., 2011). pC1 activated flies show enhanced object pursuit behavior that persists for several minutes (Agrawal et al., 2014; Bath et al., 2014; Inagaki et al., 2014; Kohatsu and Yamamoto, 2015; Rezával et al., 2016), suggesting strong potentiation of the downstream locomotor control circuit. Our findings reveal a circuit configuration where pC1 may gate/potentiate the LC-P9 sensorimotor loop (Figure 3F), leading to context-specific object directed walking. Consistent with this, recent studies demonstrated that LC10 neurons participate in object tracking during courtship and proposed that LC10 and pC1 converge on downstream targets to drive object directed walking (Ribeiro et al., 2018). Although LC10 did not activate P9 (Figure 3C), it is possible that its effect on P9 is gated by pC1 activity. Similar to the P9 pathway, state-dependent gating of sensorimotor loops in *Drosophila* was recently demonstrated for a visually evoked landing circuit (Ache et al., 2019), suggesting a general circuit architecture for context-dependent, modular regulation of sensory-driven responses.

Although we defined a role for P9 in object pursuit during courtship behavior, it is unlikely that P9 neurons are the only DNs involved in walking control during courtship, as males with P9 transmission blocked are able to track females for short periods. In addition, we have not explored the role of P9 in other steering behaviors. Indeed, cricket DNs implicated

in walking control have been shown to be responsive to multiple sensory stimuli in a state-dependent fashion (Staudacher, 2001).

Bolt Protocerebral Neurons (BPNs) drive fast, straight forward walking

The ability of BPNs to drive high speed, straight forward walks (or "sprints") inspired the name "Bolt" neurons, given Usain Bolt's unmatched sprinting records. Unilateral BPN activation induced straight forward walking, in contrast to turning phenotypes elicited by unilateral activation of other walking initiation neurons (P9, MDN and cricket DNs) (Böhm and Schildberger, 1992; Sen et al., 2017; Zorovi and Hedwig, 2013). BPNs also likely function in speed control, as increasing activity increased walking speed. The activation, silencing and neural activity recording studies suggest BPNs are important when animals execute long, straight, fast walking, i.e. when the fly needs to cover a large distance in a short time. This suggests a potential role in exploratory or escape like behaviors. However, their widespread dendritic fibers in the higher brain suggest that they might integrate multiple sensory inputs and may represent higher order regulators of walking, akin to pC1 neurons for courtship control. This anatomy makes BPNs unlikely to be involved in reflexive escape behaviors (e.g. like the jumping response encoded by the giant fiber neurons). Instead, we favor the hypothesis that BPN is involved in sustained walking during certain types of exploratory behaviors (e.g., exploring new environments) or other forms of escape that require moving out of an unpleasant environment. As not all BPNs showed detectable responses during spontaneous walking (Figure S6 and STAR Methods), there may be functional subclasses within the BPN population.

The BPN pathway shows remarkable similarity to a recently described mouse MLR-caudal brainstem circuit that promotes high-speed walking: in both cases, unilateral activation induces walking initiation without a turning bias, activation strength correlates with walking speed, and reduced activity causes specific defects in high speed walking (Capelli et al., 2017, Caggiano et al, 2018). Moreover, we demonstrate that BPN is active during high-speed straight forward walks, when the animal is spontaneously walking. Taken together, these studies argue that high-speed walking is executed by specialized walking circuits that serve an essential function across different organisms.

Although BPNs are necessary for fast walking, the ability of BPNs to drive different walking speeds at different stimulation frequencies, provides an opportunity to examine downstream mechanisms for speed control. Recent studies in zebrafish (Ampatzis et al., 2014; Song et al., 2018) show a gradient of recruitment of distinct premotor circuits at increasing swimming speeds. In *Drosophila,* recent work (Azevedo et al., 2020) has characterized distinct motor neurons recruited in a similar manner as leg movements accelerate. Examining how BPNs recruit these motor programs in an intensity dependent manner will help illuminate the mechanism of walking speed control in *Drosophila.*

BPNs and P9 define novel pathways for walking control

Unlike the mammalian locomotor system which has been explored at multiple hierarchical levels like the cortex, basal ganglia, cerebellum, brain stem and spinal cord (Arber and Costa, 2018), the invertebrate walking control has been mainly investigated at the level of

the nerve cord circuits and DNs (Bässler and Büschges, 1998; Bidaye et al., 2018; Tuthill and Azim, 2018). The only higher brain structure analyzed in the context of locomotion is the central complex (CC) which has been implicated as the site for generation of an internal heading signal (Green et al., 2017, 2019; Kim et al., 2017; Seelig and Jayaraman, 2015; Turner-Evans et al., 2017). These heading signals are thought to directly influence CC output neurons involved in turning and speed control (Heinze and Pfeiffer, 2018; Martin et al., 2015; Strauss, 2002). It is unclear how CC or other higher brain areas control downstream locomotor circuits.

The P9 and BPN pathways elucidate genetically defined, specific brain neurons that drive coordinated walking behaviors. These neurons are upstream of nerve cord circuits and likely downstream or independent of CC navigation circuits. As BPNs are higher brain neurons located outside the CC and are not involved in turning behaviors, BPNs could constitute a CC independent pathway involved in non-directed high-speed forward walking, providing an important landmark in examining higher brain regions for walking control. In addition, the LC9-P9-pC1 neural circuit motif provides a model of how context impinges on locomotor decisions directly at the level of DNs. Further, because BPN and P9 activation elicits complete, distinct walking programs, they are critical nodes that will enable evaluation of how downstream locomotor circuits in the ventral nerve cord execute different walking patterns. Thus, P9 and BPN pathways reveal organization of the invertebrate walking control circuits across different hierarchical levels and provide an important advance in our understanding of how brain pathways switch on downstream walking control circuits.

STAR Methods:

RESOURCE AVAILABILITY

Lead Contact—Further information and requests for resources and reagents should be directed to and will be fulfilled by the Lead Contact, Kristin Scott (kscott@berkeley.edu)

Materials Availability—All materials generated in this study including fly lines and custom design files will be available upon request.

Data and Code Availability—Raw and processed data along with custom analysis scripts will be made available upon request.

EXPERIMENTAL MODEL AND SUBJECT DETAILS:

Drosophila melanogaster control and transgenic lines used in this study are described in detail in Key Resources Table. Table S1 documents genotypes used for each figure. Flies were raised in vials containing standard cornmeal-agar medium supplemented with baker's yeast and incubated at 25°C with 60% humidity and 12h light/dark cycle throughout development and adulthood unless otherwise stated. The behavioral screen and all optogenetic activation experiments were performed in female flies aged 7–10 days unless otherwise stated. For stochastic activation experiments, crosses were set at 19°C. and the larvae were heat shocked during development for 1.5 to 2 hrs at 37°C. All optogenetic activation experimental flies were collected on retinal food and again transferred to fresh

retinal food 1–2 days prior to testing. Retinal food contains standard fly food with freshly added 400 μM all-trans retinal. These flies were kept in the dark from eclosion until test. The courtship experiments were performed using 8–10 day old test males paired with 5–6 day old virgin females. The males were collected as virgins and raised in isolation in 1.5 ml Eppendorf vials with ~ 0.75ml standard food and holes for air exchange.

METHOD DETAILS:

Fly Genetics: All DN split-Gal4 lines used in the screen were generously provided pre-publication by S.Namiki and G.Card (Namiki et al., 2018). The VT and GMR generation 1 *Gal4* lines were obtained from Vienna *Drosophila* Resource Center (VDRC) and Bloomington *Drosophila* Stock Center (BDSC) respectively. The new split-Gal4 lines for P9 and BPNs were created using color MIP masked search on the entire registered image database (Dionne et al., 2018; Otsuna et al.2018; Tirian and Dickson, 2017) made available by Janelia Research Campus. Candidate drivers targeting the neurons of interest were identified and corresponding split-Gal4 hemi-drivers were obtained from BDSC. Sources for other reagents used are described in Table S1 and Key Resources Table. Detailed information about all genotypes used in the screen is available on request.

Activation Screen: All behavioral experiments were performed in a temperature and humidity-controlled room (25°C, 60% humidity). The behavioral arenas were designed by pouring 1.5% agarose gel in a regular 150 mm petri-plate with 3D printed acrylic molds designed for generating bowl-shaped behavioral arenas. The arenas were covered with a glass ceiling painted with Sigmacote. Four bowl-shaped arenas of 44 mm diameter were imaged with one camera (JVC camcorder GZ-E300AU) at a resolution of 1920×1080 and 30 fps. Four cameras operated in parallel during the screen. The arena was backlit with custom designed bright white LED panels and the light was on throughout the assay. Intensity was adjusted using *MDN-1>CsChrimson* (Bidaye et al., 2014) as a positive control. For long duration continuous stimulation, white light of 0.5 mW/cm^2 at the arena walking surface was sufficient to observe CsChrimson phenotypes. Powdered and clean flies were tested for each genotype. The powdered flies were coated with fine yellow dust (Reactive Yellow 86, Cat # sc-296260), (Seeds et al., 2014) just prior to loading them into the behavioral arena. A 7 minute video was acquired after flies acclimatized to the behavioral arena for 3 minutes (dim lights).

Transient Activation Setup: A custom LED plate was designed as a backlight for optogenetic experiments. The plate (150 mm X 150 mm) consists of high density high power LEDs (10×10 LED positions); 3 LEDs per position, 870nm, 630nm and 530nm, each with an independent intensity control, a switch input and a TTL input for pulsing at desired frequencies. The panel was placed underneath a diffuser sheet to provide even illumination at the arena walking surface. The 870nm IR LED was switched ON at low intensity throughout the assay. For CsChrimson activation experiments, 630nm LED was adjusted to output ~4.5 mW/cm^2 intensity at the arena walking surface and was transiently switched on and pulsed at 50Hz (5ms pulse width) via the TTL input unless otherwise stated. For the green light walking induction experiments, the 530 nm green LED was adjusted to output ~1.8mW/cm^2 intensity at the arena walking surface and transiently

switched on during the assay. Videos in this setup were acquired using a FLIR Blackfly S camera (FL3-U3–13Y3M-C) at a resolution of 1280 X 1024 at 30 fps. The camera was fitted with an adjustable focus lens (LMVZ990-IR) and NIR bandpass filter (Midopt BP850) to allow IR imaging without artifacts from visible light. All transient activation experiments (unless otherwise stated) were performed in the dark.

Transient Activation Grooming Assay: Powdered flies loaded in bowl-shaped arenas described above were assayed for walking initiation on transient activation in the above setup. The light stimulation protocol consisted of 60s OFF 30s ON sequence, repeated 3 times. For analysis, 30s OFF followed by 30s ON was considered as one trial.

Transient Activation Copulation Assay: Virgin test females were paired with Canton S wild type males in the bowl-shaped arena described above and allowed to begin copulation. Once copulation was initiated, the light stimulation protocol of 30s OFF 10s ON was repeated 3 times. Longer assay duration or light ON periods often led to unmounting. For analysis, 8s OFF followed by 8s ON was considered as one trial. In the event of rare unmounting during the assay, that video was discarded from the analysis.

<u>Courtship Assay:</u> We paired Canton S virgin females with test males in bowl-shaped arenas described above placed on top of white LED backlight (0.5 mW//cm^2). 10 minute videos were acquired using JVC camcorders (GZ-E300AU) at 1920× 1080 resolution and 30 fps.

<u>Remote-controlled female courtship assay:</u> Virgin *SS01540>CsChrimson(attp18)* females (aka remote-controlled females or P9>Chr) were paired with test males in bowl shaped arenas and placed in the transient activation setup. Diffuse room lighting provided enough light to increase courtship compared to lights OFF, indicating that visual aspects of courtship were functional. During the assay, the remote-controlled females were triggered to initiate high forward and angular velocity walking by transiently switching on the 630nm light (10s OFF 20s ON for a total of 10 minutes). 10 minute videos were recorded using the FLIR BlackFlyS camera at 1280 X 1024 and 30 fps.

<u>Flat arena Courtship Assay:</u> *Canton S* virgin females were paired with test males in flat floor arenas designed to increase complex following events. These arenas are 50mm diameter and 3 mm high with serrated walls. Arena floor is a diffuser sheet placed on hard clear acrylic sheet. The arenas were backlit with white LEDs (0.5mW/cm^2) and 10 min videos were recorded using JVC camcorder at 1920× 1080 resolution and 30 fps.

<u>Freezing Assay:</u> For reproducing the P9 freezing phenotype we designed an arena as similar to the published one (Zacarias et al., 2018) as possible. The main difference from our usual bowl shaped arena was that the floor of these arenas was hard flat acrylic instead of curved agarose floor. These arenas were identical in dimensions to the flat shaped courtship arena described above except these arenas did not have serrated walls, so that flies could also walk on the arena walls, similar to Zacarias et al assay. The LED intensity and pulsing durations were adjusted to be similar to Zacarias et al assay, viz. ~2.5 mW/cm^2 intensity and

10 repetitions of 2s light ON (continuous on without pulsing) followed by 10s light OFF period.

Green Light Induced Walking Assay: Test flies were aspirated in flat arenas and placed in the transient activation setup. The flat courtship arenas were used, so that baseline walking velocity was low allowing us to see an increase in walking velocity with green light. Green light was switched on transiently (60s OFF 30s ON) for three trials and videos were recorded on FLIR BlackFlyS camera at 1280 X 1024 at 30 fps.

BPN walking assay: Same conditions as green light assay, except that green light was not turned on during the 10 minute video recording.

High resolution walking assay: The setup consisted of an inverted glass petri dish that we used as a transparent arena (diameter 80 mm) held by a circular frame with a cutout below the dish. The cutout provided an unobstructed bottom view of the arena. A surface mirror was placed below the arena at a 45° angle. An infrared (IR)-sensitive high-speed camera (model VC-2MC-M340; Vieworks, Anyang, Republic of Korea) focused on this mirror was used to image a bottom view of a central 30mm x 30mm square on the surface of the arena, at a resolution of 1000 by 1000 pixels and frame rate of 200 Hz (exposure time of 200 μs). Illumination was provided by a ring of 60 IR light-emitting diodes (LEDs, wavelength: 870 nm) arranged concentrically around the arena and emitting their light mainly parallel to the arena's surface. This resulted in a strong contrast between background and fly (see Figure S4A). Contrast and homogeneity were further increased by equipping the camera's lens with an IR-pass filter (cut-off frequency: 760 nm) that blocked all ambient visible light. The LED activity was pulsed and synchronized to frame acquisition of the camera. To prevent flies from escaping, the arena was covered with a watch glass that established a dome-shaped enclosure, similar to an inverted FlyBowl (Simon & Dickinson, 2010). To prevent flies from walking upside down on the watch glass, we covered its inside surface with SigmaCote (Sigma-Aldrich, St. Louis, MO). Prior to an experiment, a single fly was extracted with a suction tube from its rearing vial, cold-anesthetized for approximately one minute, and placed onto the arena, which was then covered with the watch glass. Flies were allowed to regain mobility and then acclimatize for ~15 minutes, after which video acquisition was started.

Flies walked spontaneously for several hours in the arena and frequently crossed the capture area. Video data of this area was continuously recorded into a frame buffer of 5–10s duration. During an experiment, custom-written software functions evaluated the recorded frames online and determined if a fly was present at a particular time and if it had produced a continuous walking track that had a minimum length of 7 BL (body lengths) and a minimum walking speed of 2 BL/s. Once the fly had produced such a track and then either stopped or left the capture area, the contents of the frame buffer were committed to storage as a trial for further evaluation and analysis. Video acquisition and online evaluation during experiments were implemented in MATLAB 2018b (The MathWorks, Natick, MA).

Immunohistochemistry: Staining of fly brain and ventral nerve cord was performed as described previously (Yu et al., 2010). Briefly, flies were dissected in cold PBS and

brains and VNCs were fixed in 4% PFA. This was followed by PBST washes, then blocking in normal goat serum, followed by primary antibody incubation for 2 days, PBST washes and secondary antibody incubation for another 2 days. The stained tissues were then mounted in Vectashield and imaged under LSM 780 system using the 1P excitation and emission corresponding to the secondary antibodies used. Antibodies are as described in Key resources table. Primary antibodies were used at 1:500 or 1:1000 dilution and secondaries were used at 1:500 dilution.

Neuron morphology segmentation: For P9 and LC9 neuron segmentation we used the publicly available split-gal4 resource (Namiki et al., 2018; Wu et al., 2016) and registered it on the JFRC2 template using the CMTK toolkit. For pC1 we used the JFRC2 template registered pMP-e image obtained from virtualFlyBrain resource (Cachero et al., 2010; Osumi-Sutherland et al., 2014). For BPN, we registered our nc82 co-stained image of *BPN-S1>CsChrimson* on the JFRC2 template using the CMTK toolkit (Jefferis et al., 2007). The neuron segmentations were created using the registered images in VVD software (Otsuna et al., 2018). VVD was also used for visualizing potential overlap between the segmented neurons and creating the segmented neuron figures.

CsChrimson quantification: 8–9 day old female flies were cold anesthetized and brains were dissected in cold Artificial Hemolymph (AHL) solution (Wang et al., 2004). The brains were then transferred on a PLL coated coverslip posterior side up and immersed in AHL. CsChrimson-mVenus expression was detected using 514nm confocal laser scanning of region of interest under a 20x NA 0.8 objective lens on a LSM 880 Zeiss microscope. For P9 CsChrimson analysis, zoomed in 3D stack comprising the entire soma was captured. For gamma lobe CsChrimson analysis, 3D ROI consisting of the neurites was imaged. This entire data set (Figure S2 G) was obtained by imaging age matched flies using identical imaging parameters during the same imaging session.

Functional Connectivity: Functional connectivity experiments were performed in freshly dissected explant brains under a LSM 880 two photon microscope using 20x NA =0.8 objective lens. Brains and connected VNC were dissected and imaged in extracellular saline (ECS) solution (103mM NaCl, 3mM KCl, 5mM N-tris(hydroxymethyl) methyl-2-aminoethane-sulfonic acid, 10mM trehalose, 10mM glucose, 2mM sucrose, 26mM $NaHCO_3$, 1mM NaH_2PO_4, 1.5mM $CaCl_2$, and 4mM $MgCl_2$, adjusted to 275 mOsm, pH equilibrated near 7.3 when bubbled with carbogen). The explant was placed on PLL coated coverslip in an imaging chamber (ALAMS-518SWPW). ECS bubbled with carbogen was perfused over the brains throughout the imaging session. To activate Chrimson, 650 nm red light was delivered to the sample through the objective. A BP excitation filter centered around 655nm and custom notch dichroic (Chroma ZT656dcrb) delivered the red light on the sample and the dichroic at the same time allowed transmission of the 920nm imaging laser as well as the green GCaMP signal back to the detectors. The activation light LED was controlled via TTL inputs synchronized to the imaging session using ZEN2.0 software and an external trigger box plus a signal generator. A given session consisted of three to five activation trials consisting of 30s OFF 10s ON periods. During the ON period, the LED was pulsed at 50 Hz (2ms pulse duration). 512×512 pixel images were acquired at 3 to 4 Hz. A

high intensity two color 1P confocal stack was acquired at the end of the imaging session to confirm expression. In case of samples that showed GCaMP responses, the brains from the same batch of flies were immunostained to confirm there was no co-expression of Chrimson and GCaMP in the same neuron (Figure S3A,B).

Anatomical connectivity in the EM hemibrain data: The recently released Electron Microscopy hemibrain data version 1.0.1 (Meissner et al., 2020) was mined to verify the anatomical correlates of our functional connectivity results, using the "neuPrint Explorer" tool. Since LC9 and pC1 neuronal classes were already traced and annotated in this data, these were used as starting points. Given this is a female *Drosophila* brain connectome, the sexually dimorphic pC1 class contains 5 cells versus 60 cells in males. Therefore, the LC9 neuronal type was first used to search for potential downstream candidates that resemble P9 both with respect to cell body position and neurites. Cell ID 1228264951 was identified as potential candidate given its strong connectivity to LC9 and anatomical similarity to P9. The EM skeleton of this cell was then compared to large database of light microscopy images using "NeuronBridge" (Xu et al., 2020) tool. This unbiased image search provided a perfect match (highest ranked hit with a score of 50000) between cell ID 1228264951 and expression pattern of *SS01540* (the P9 split-Gal4 reagent). This confirms that we identified P9 in the EM data. NeuPrint Explorer tools were then used to probe direct and indirect connections between pC1, LC11 and P9 and led to identification of several direct and indirect connections (summarized in Figure 3E) that validate our functional connectivity results.

***In-vivo* Imaging:** Imaging in tethered walking flies was performed on a 3i spinning disc confocal system with a 20x water immersion objective (NA 1.0). Male flies (age 5–7) were cold anesthetized and attached on a custom holder, modified version of (Weir et al., 2016). The head was positioned such that the ocelli were on the top and covered with AHL. The holder ensured that only the superior dorsal part of the head was immersed in the solution leaving the antennae and proboscis dry. The proboscis was glued to reduce brain movement. A small hole was created in the cuticle encircling the ocelli region and air sacs were removed. The holder was then placed under a 20x objective and imaged using a 488nm laser. This dissection revealed BPN soma; however, since the soma are positioned along the curved top surface of the brain, not all soma could be imaged in all samples. For P9 imaging, a larger area of cuticle was removed to access P9 soma. Once the imaging ROI was centered, an air supported ball was positioned under the fly using micromanipulators. The track-ball (polypropylene, diameter: 6 mm, Spherotech GmbH, Germany). freely floated on a controlled air stream through a ball holder (Berendes et al., 2016; Seelig et al., 2010). Two cameras placed at right angle to each other were used to carefully align a square sleeve placed on the ball holder such that it aligned with the axis of the fly (Green et al., 2017). This was later used to determine the coordinate frame of the fly via FicTrac (Moore et al., 2014). The ball was illuminated with 850nm IR LED and imaged using a FLIR BlackFly S Camera and lens mentioned in the above section. Video was acquired at 400×400 resolution and 50fps and was synchronized to the imaging session via slidebook software and a TTL trigger input to the camera. Once the fly was acclimatized to the ball and started walking, a volume consisting of the BPN soma was imaged at frame rate of 0.5–0.9 Hz.

Imaging sessions of walking flies usually lasted 5–7 minutes. The synchronized GCaMP imaging and ball tracking data was then analysed offline. For a subset of sessions, dual color imaging of both GCaMP and RFP was performed (Figure S6D–I). The low uncorrelated RFP imaging data confirms that GCaMP changes are not due to movement artifacts. Since GCaMP and RFP bleach at different rates during these long 1P imaging sessions, we did not perform ratiometric analysis.

QUANTIFICATION AND STATISTICAL ANALYSIS:

All data analysis was performed in Matlab and statistical tests were performed in Graphpad Prism. Graphs were plotted either in Matlab or Graphpad.

Analysis of walking during activation and silencing assays.—Videos were processed using a custom batch processing script that cropped videos into single arena videos and uncompressed to avi format. These preprocessed videos were then tracked using FlyTracker software (Eyjolfsdottir et al., 2014). The tracker returned the centroid position of the fly, orientation and instantaneous translational velocity. For the activation screen, we focused solely on the translational velocity parameter. Since the screen spanned several days of experiments, a control video *(UAS-CsChrimson*X *w1118)* of both clean and powdered flies (n = 16 each) was recorded on each test day. All test fly data was then normalized with respect to the day control for visualizing outlying clusters (Figure 1B and S1A). The orientation attribute was used to determine the signed or absolute angular velocity of the fly. All plots except for stochastic activation experiments report the absolute angular velocity of the fly. We calculated angular velocity, translational velocity, distance traveled and total angular rotation (area under the curve of absolute angular velocity) for each trial and then averaged the trials for plotting and statistical analysis of per fly attributes. Straightness or Straightness Index (SI) was a modified version of a previously reported definition (Cruz et al.) and calculated for first 4 seconds of optogenetic activation for the trial that showed longest distance covered. In order to calculate straightness without any effect of velocity we defined SI as a pure spatial parameter. For every point on the trajectory, 6 mm trajectory segment centered around that point was extracted (spatial window) and SI for that segment was calculated as trajectory length divided by the sum of deviations from an ideal path (i.e. a straight line joining the first and last points in that window). Straight paths have small deviations from ideal path and hence larger value of SI. Trajectories less than 6mm were rare and discarded from analysis. Distance, total rotation and straightness values were primarily used for statistical analysis and velocity profiles were used for showing the dynamics of the activation phenotype. In all transient activation data figures, n represents number of flies and the values for n and statistical analysis is described in the figure legends.

Walking bout pooled analysis for BPN silencing experiments: Walking bouts were defined as continuous time periods with smoothed translational velocity above 1.5 mm/s. For each bout we calculated bout duration, mean translational velocity and mean angular velocity. All control and *BPN>TeTx* bout data were pooled and z-scored for normalization and plotting and analyzing the V_T versus T_W distribution and (Figure S6B,C). The cutoff at z-score=2 was chosen as a conservative threshold to obtain bouts with unusually high V_T and/or T_W attributes.

Courtship Assays: The courtship videos were preprocessed and tracked using FlyTracker as described above. The two-fly tracking output was manually checked for fly identity mismatch using "visualizer" script in the FlyTracker software and any mismatch was corrected. The centroid positions and orientations of the flies were used to calculate the distance between the two flies and the angle between the male and female as per previous reports (Ribeiro et al., 2018). The following Index was defined as fraction of pre-copulation time spent by the male within 5 mm of female and oriented towards the female (angle < 30) (Ribeiro et al., 2018). Velocity correlation was the correlation between the translational velocities of male and female fly in a given courting pair before copulation. Probability density functions of distance and angle between the courting pair were calculated per courting pair and then plotted as mean ± SEM for visualization. All genotypes and the corresponding GAL4 controls were tested on the same day. The entire data set for each assay represented across Figures 4 and S3 were analyzed together. (note there was only 1 empty split Gal4 control group for each assay but control data was replotted in Figure S3 E,F for comparison with tests that were not shown in Figure 4 B,D,F)

CsChrimson expression quantification: Mean fluorescence intensity was quantified for each ROI (P9 soma or gamma lobe neurites). Data for all flies imaged was reported. The gamma lobe expression was only present and quantified in the SS01540 line.

Functional Connectivity: Mean ROI fluorescence of P9 soma and a background ROI was calculated using ImageJ. Background subtracted fluorescence intensity was used to calculate   F/F0 where F0 is calculated as mean fluorescence during 10s prestimulation light OFF period. We plotted data for 10s OFF 10s ON and 10s OFF for each trial. Area under the curve during light ON period was used for statistical analysis.

In-vivo imaging: GCaMP6 imaging data was analyzed using open source and custom Matlab scripts. The NormCorre Matlab package (Pnevmatikakis and Giovannucci, 2017) was used for image registration to remove movement artifacts. ROIs were manually drawn around each visible BPN soma, ignoring somas close to Z-stack boundary plane to avoid movement artifact, and mean ROI fluorescence was extracted. This pre ROI fluorescence data was then bleach corrected using the bleach correction script from CaImAn-MATLAB toolbox (Giovannucci et al., 2019). The AF/F0 values (threshold 0.1 and 10–90 percentile range > 0.2) for each ROI were used to filter out soma that did not show activity during the imaging session. 5 of 9 soma for fly1, 3 of 5 soma for fly2 and 3 of 8 soma for fly3 we defined as active. The bleach corrected BPN soma fluorescence data was then z-scored and used for further analysis. The mean BPN activity data was mean of z-scored bleach corrected fluorescence for all active soma.

The ball movement was tracked offline using FicTrac software (Moore et al., 2014). FicTrac directly provided the position of the fly in a virtual space as well as the instantaneous translational velocity and virtual heading of the fly. These attributes were used for calculating angular velocity, walking bout duration and straightness index. SI is as defined in the previous section except the spatial window (12mm) used for tethered fly walking, differed from free-walking assay described earlier. Also, because SI was not defined using a

temporal window, we did not include SI as an attribute in the linear model or clustering of other time series attributes.

The low frame rate GCaMP imaging data were upsampled (interpolated to high frame rate of 1kHz and then digitized to 50 Hz) to match the ball tracking frame rate for data analysis. The behavioral attributes were convolved using a GCaMP6s kernel (Turner-Evans et al., 2017) and the obtained regressors were used for calculating correlations and generating a linear regression model. Although correlations of BPN activity with behavioral regressors could be obtained, the slow <1Hz imaging frame rate made it difficult to make any claim about the lag between the two variables.

For pooled data analysis across flies and imaging sessions, data for each imaging session was first divided into walking bouts defined as any continuous walking event ($V_T > 2$ mm/s). Then the z-scored mean BPN activity and behavioral attributes (V_T, V_A, T_W) were clustered using k-means clustering into 3 clusters. To visualize the BPN activity dynamics for each cluster, we aligned the BPN activity data to walking bout initiation frame and plotted mean BPN activity before and after bout initiation for each cluster separately as mean ± SEM bounded plots (Figure 6J).

High resolution walking analysis: Prior to data analysis, walking sequences which had low within-trial variability in walking speed (translational velocity) and in which flies walked in a straight line with at least five consecutive steps were selected. These pre-selected sequences served as the basis for further analysis of low-level walking-related parameters. First, the position of the fly throughout a sequence was determined automatically. In brief, each video frame was converted into a binary image (black background, bright fly), in which, following a simple threshold operation, the fly was detected as the largest bright area. The walking speed was calculated as changes of the center of mass of this area over time. This positional information was used to crop the fly from the original 1000 by 1000-pixel video. These smaller and fly-centered video sequences were used for the annotation of eight different body parts in every video frame: the tarsal tips of all six legs, the neck, and the posterior tip of the abdomen (Figure. S4A). This step of the annotation was done automatically in DeepLabCut (DLC, Mathis et al, 2018); to use this approach we trained and evaluated DLC with a data set of 1000 manually annotated video frames (10 flies, 100 exemplary frames each), that were similar to the ones we recorded during the experiments described here. One half (500 frames, 10 flies, 50 frames each) of this set was used for training DLC, the other half was used to evaluate its performance. Performance of DLC was generally very good; however, to ensure high-quality annotations the results were inspected manually and, if necessary, corrected.

To determine the times of lift-off and touch-down for each leg in a walking sequence, the DLC-determined positions of the tarsal tips were transformed into a world-centered coordinate system. In this coordinate system, a leg tip is stationary, i.e. has a speed of zero, when the leg is touched down (here, defined as the stance movement) and moves markedly with regard to the ground when it is lifted off (here, defined as the swing movement). These measures and an empirically determined threshold were used to distinguish between swing and stance movement. Transitions between these two were defined as touch down

and lift off events, respectively, and the positions of the tarsal tip at these times were defined as the anterior and posterior extreme positions (AEPs and PEPs) in fly-centered coordinates, respectively. A single step of a particular leg was then defined as its movement between two subsequent PEPs; its period was defined as the time difference between two subsequent PEPs. Swing movement and duration were defined as the movement and the time difference, respectively, between a PEP and the subsequent AEP; stance movement and duration were defined as the movement and the time difference, respectively, between an AEP and the subsequent PEP. A stance trajectory was defined as the complete path of a tarsal tip in fly-centered coordinates between an AEP and the subsequent PEP. Step amplitude was defined as the distance between a PEP and the subsequent AEP. Stance linearity was calculated as the root mean squared error (RMSE) between an actual stance trajectory and a straight line between this stance trajectory's AEP and PEP; the higher this measure is the stronger the deviation from a straight line. Average AEPs and PEPs were defined as the arithmetic mean of all AEP and PEP position vectors, respectively; the standard deviation of these positions were estimated as a bivariate distribution. Stance trajectories were averaged by first re-sampling all n trajectories to 100 equidistant positions and then calculating the arithmetic mean for each set of n-by-100 data points. To facilitate comparison between control and experimental condition all individual step periods, swing durations, stance durations, stance amplitudes, and stance linearity values were normalized to the arithmetic mean of the control condition.

Phase relationships, i.e. phase differences, were calculated for all ipsilaterally or contralaterally adjacent leg pairs (Figure S4B). This resulted in seven phase relationships: three contralateral leg pairs (front, middle, and hind legs), as well as four ipsilateral leg pairs (hind and middle legs, and middle and front legs, respectively). For each leg pair a reference leg was selected. For contralateral phase relationships this was a left leg, for ipsilateral phase relationships this was the posterior leg. For each complete step of the reference leg (i.e. PEP to PEP) its instantaneous phase was calculated as a value that linearly increased from 0 to 1 during the step. The phase relationship between the two legs was then calculated as the phase value at the times of PEPs in the non-reference leg; this is equivalent to the phase difference between these legs. A value of 0 indicates synchronous lift off, for instance, while a value of 0.5 would indicate exactly anti-phase. The phase between two legs is indicated by, for instance, R3>R2, where the right hind leg (R3) is the reference leg and R2 (the right middle leg) is the non-reference leg (Figure S4B).

All annotations and calculations, apart from DLC-based functions, were carried out with custom-written functions in MATLAB 2018b.

Supplementary Material

Refer to Web version on PubMed Central for supplementary material.

Acknowledgments

References:

Ache JM, Haupt SS, and Dürr V.(2015). A direct descending pathway informing locomotor networks about tactile sensor movement. J. Neurosci 35, 4081–4091. [PubMed: 25740535]

Ache JM, Namiki S, Lee A, Branson K, and Card GM (2019). State-dependent decoupling of sensory and motor circuits underlies behavioral flexibility in *Drosophila*. Nat. Neurosci 22, 1132–1139. [PubMed: 31182867]

Agrawal S, and Dickinson MH (2019). The effects of target contrast on *Drosophila* courtship. The Journal of Experimental Biology 222, jeb203414.

Agrawal S, Safarik S, and Dickinson M.(2014). The relative roles of vision and chemosensation in mate recognition of *Drosophila melanogaster*. J. Exp. Biol 217, 2796–2805. [PubMed: 24902744]

Ampatzis K, Song J, Ausborn J, and El Manira A.(2014). Separate microcircuit modules of distinct v2a interneurons and motoneurons control the speed of locomotion. Neuron 83, 934–943. [PubMed: 25123308]

Aptekar JW, Keleç MF, Lu PM, Zolotova NM, and Frye MA (2015). Neurons forming optic glomeruli compute figure-ground discriminations in *Drosophila*. J. Neurosci 35, 7587–7599. [PubMed: 25972183]

Arber S, and Costa RM (2018). Connecting neuronal circuits for movement. Science 360, 1403–1404. [PubMed: 29954969]

Azevedo AW, Dickinson ES, Gurung P, Venkatasubramanian L, Mann RS, and Tuthill JC (2020). A size principle for recruitment of Drosophila leg motor neurons. Elife 9, 10.7554/eLife.56754.

Bässler U, and Büschges A.(1998). Pattern generation for stick insect walking movements-- multisensory control of a locomotor program. Brain Res. Brain Res. Rev 27, 65–88. [PubMed: 9639677]

Bath DE, Stowers JR, Hörmann D, Poehlmann A, Dickson BJ, and Straw AD (2014). FlyMAD: rapid thermogenetic control of neuronal activity in freely walking *Drosophila*. Nat. Methods 11, 756–762. [PubMed: 24859752]

Berendes V, Zill SN, Büschges A, and Bockemühl T.(2016). Speed-dependent interplay between local pattern-generating activity and sensory signals during walking in *Drosophila*. J. Exp. Biol 219, 3781–3793. [PubMed: 27688052]

Berg EM, Hooper SL, Schmidt J, and Büschges A.(2015). A leg-local neural mechanism mediates the decision to search in stick insects. Curr. Biol 25, 2012–2017. [PubMed: 26190069]

Bidaye SS, Machacek C, Wu Y, and Dickson BJ (2014). Neuronal control of *Drosophila* walking direction. Science 344, 97–101. [PubMed: 24700860]

Bidaye SS, Bockemühl T, and Büschges A.(2018). Six-legged walking in insects: how CPGs, peripheral feedback, and descending signals generate coordinated and adaptive motor rhythms. J. Neurophysiol 119, 459–475. [PubMed: 29070634]

Böhm H, and Schildberger K.(1992). Brain Neurones Involved in the Control of Walking in the Cricket Gryllus Bimaculatus. J. Exp. Biol 166, 113–130.

Bouvier J, Caggiano V, Leiras R, Caldeira V, Bellardita C, Balueva K, Fuchs A, and Kiehn O.(2015). Descending Command Neurons in the Brainstem that Halt Locomotion. Cell 163, 1191–1203. [PubMed: 26590422]

Brown TG (1911). The Intrinsic Factors in the Act of Progression in the Mammal. Proceedings of the Royal Society B: Biological Sciences 84, 308–319.

Burdohan JA, and Comer CM (1996). Cellular Organization of an Antennal Mechanosensory Pathway in the Cockroach,Periplaneta americana. The Journal of Neuroscience 16, 5830–5843. [PubMed: 8795635]

Büschges A, Schmitz J, and Bässler U.(1995). Rhythmic patterns in the thoracic nerve cord of the stick insect induced by pilocarpine. J. Exp. Biol 198, 435–456. [PubMed: 9318078]

Bässler U.(1976). Reversal of a reflex to a single motoneuron in the stick insect Carausius morosus. Biological Cybernetics 24, 47–49.

Cachero S, Ostrovsky AD, Yu JY, Dickson BJ, and Jefferis GSXE (2010). Sexual dimorphism in the fly brain. Curr. Biol 20, 1589–1601. [PubMed: 20832311]

Caggiano V, Leiras R, Goñi-Erro H, Masini D, Bellardita C, Bouvier J, Caldeira V, Fisone G, and Kiehn O.(2018). Midbrain circuits that set locomotor speed and gait selection. Nature 553, 455–460. [PubMed: 29342142]

Cande J, Namiki S, Qiu J, Korff W, Card GM, Shaevitz JW, Stern DL, and Berman GJ (2018). Optogenetic dissection of descending behavioral control in *Drosophila*. eLife 2018;7:e34275

Capelli P, Pivetta C, Soledad Esposito M, and Arber S.(2017). Locomotor speed control circuits in the caudal brainstem. Nature 551, 373–377. [PubMed: 29059682]

Carreira-Rosario A, Zarin AA, Clark MQ, Manning L, Fetter RD, Cardona A, and Doe CQ (2018). MDN brain descending neurons coordinately activate backward and inhibit forward locomotion. eLife 2018;7:e38554

Chen C-L, Hermans L, Viswanathan MC, Fortun D, Aymanns F, Unser M, Cammarato A, Dickinson MH, and Ramdya P.(2018). Imaging neural activity in the ventral nerve cord of behaving adult *Drosophila*. Nat. Commun 9, 4390. [PubMed: 30348941]

Cheng J, Stein RB, Jovanovic K, Yoshida K, Bennett DJ, and Han Y.(1998). Identification, localization, and modulation of neural networks for walking in the mudpuppy (Necturus maculatus) spinal cord. J. Neurosci 18, 4295–4304. [PubMed: 9592106]

Clowney EJ, Iguchi S, Bussell JJ, Scheer E, and Ruta V.(2015). Multimodal Chemosensory Circuits Controlling Male Courtship in *Drosophila*. Neuron 87, 1036–1049. [PubMed: 26279475]

Coen P, Xie M, Clemens J, and Murthy M.(2016). Sensorimotor Transformations Underlying Variability in Song Intensity during *Drosophila* Courtship. Neuron 89, 629–644. [PubMed: 26844835]

Cook R.(1980). The extent of visual control in the courtship tracking of D. melanogaster Biological Cybernetics 37, 41–51.

Crickmore MA, and Vosshall LB (2013). Opposing dopaminergic and GABAergic neurons control the duration and persistence of copulation in *Drosophila*. Cell 155, 881–893. [PubMed: 24209625]

Cruz T, Fujiwara T, Varela N, Mohammad F, Claridge-Chang A, and Eugenia Chiappe M.(2019) Motor context coordinates visually guided walking in Drosophila. bioRxiv 10.1101/572792

DeAngelis BD, Zavatone-Veth JA, and Clark DA (2019). The manifold structure of limb coordination in walking *Drosophila*. eLife 8:e46409

Dickson BJ (2008). Wired for sex: the neurobiology of *Drosophila* mating decisions. Science 322, 904–909. [PubMed: 18988843]

Dionne H, Hibbard KL, Cavallaro A, Kao J-C, and Rubin GM (2018). Genetic Reagents for Making Split-GAL4 Lines in. Genetics 209, 31–35. [PubMed: 29535151]

Eyjolfsdottir E, Branson S, Burgos-Artizzu XP, Hoopfer ED, Schor J, Anderson DJ, and Perona P.(2014). Detecting Social Actions of Fruit Flies. Computer Vision – ECCV 2014 772–787.

Giovannucci A, Friedrich J, Gunn P, Kalfon J, Brown BL, Koay SA, Taxidis J, Najafi F, Gauthier JL, Zhou P, et al. (2019). CaImAn an open source tool for scalable calcium imaging data analysis. eLife 8:e38173

Green J, Adachi A, Shah KK, Hirokawa JD, Magani PS, and Maimon G.(2017). A neural circuit architecture for angular integration in *Drosophila*. Nature 546, 101–106. [PubMed: 28538731]

Green J, Vijayan V, Mussells Pires P, Adachi A, and Maimon G.(2019). A neural heading estimate is compared with an internal goal to guide oriented navigation. Nat. Neurosci

Grillner S, and Zangger P.(1975). How detailed is the central pattern generation for locomotion? Brain Research 88, 367–371. [PubMed: 1148835]

Guschlbauer C, Gruhn M, and Daun-Gruhn S.(2012). A neuromechanical model for the neuronal basis of curve walking in the stick insect. Journal of.

Hägglund M, Dougherty KJ, Borgius L, Itohara S, Iwasato T, and Kiehn O.(2013). Optogenetic dissection reveals multiple rhythmogenic modules underlying locomotion. Proc. Natl. Acad. Sci. U. S. A 110, 11589–11594.

Heinze S, and Pfeiffer K.(2018). The Insect Central Complex – From Sensory Coding to Directing Movement (Frontiers Media SA).

Hoopfer ED, Jung Y, Inagaki HK, Rubin GM, and Anderson DJ (2015). P1 interneurons promote a persistent internal state that enhances inter-male aggression in *Drosophila*. eLife 2015;4:e11346

Inagaki HK, Jung Y, Hoopfer ED, Wong AM, Mishra N, Lin JY, Tsien RY, and Anderson DJ (2014). Optogenetic control of *Drosophila* using a red-shifted channelrhodopsin reveals experience-dependent influences on courtship. Nat. Methods 11, 325–332. [PubMed: 24363022]

Jefferis GSXE, Potter CJ, Chan AM, Marin EC, Rohlfing T, Maurer CR Jr, and Luo L.(2007). Comprehensive maps of *Drosophila* higher olfactory centers: spatially segregated fruit and pheromone representation. Cell 128, 1187–1203. [PubMed: 17382886]

Jenett A, Rubin GM, Ngo T-TB, Shepherd D, Murphy C, Dionne H, Pfeiffer BD, Cavallaro A, Hall D, Jeter J, et al. (2012). A GAL4-driver line resource for *Drosophila* neurobiology. Cell Rep. 2, 991–1001. [PubMed: 23063364]

Jordan LM, Liu J, Hedlund PB, Akay T, and Pearson KG (2008). Descending command systems for the initiation of locomotion in mammals. Brain Res. Rev 57, 183–191. [PubMed: 17928060]

Kallman BR, Kim H, and Scott K.(2015). Excitation and inhibition onto central courtship neurons biases *Drosophila* mate choice. eLife 4, e11188.

Kele MF, and Frye MA (2017). Object-Detecting Neurons in Drosophila. Curr. Biol 27, 680–687. [PubMed: 28190726]

Kim SS, Rouault H, Druckmann S, and Jayaraman V.(2017). Ring attractor dynamics in the *Drosophila* central brain. Science 356, 849–853. [PubMed: 28473639]

Klapoetke NC, Murata Y, Kim SS, Pulver SR, Birdsey-Benson A, Cho YK, Morimoto TK, Chuong AS, Carpenter EJ, Tian Z, et al. (2014). Independent optical excitation of distinct neural populations. Nat. Methods 11, 338–346. [PubMed: 24509633]

Klapoetke NC, Nern A, Peek MY, Rogers EM, Breads P, Rubin GM, Reiser MB, and Card GM (2017). Ultra-selective looming detection from radial motion opponency. Nature 551, 237–241. [PubMed: 29120418]

Klaus A, Martins GJ, Paixao VB, Zhou P, Paninski L, and Costa RM (2017). The Spatiotemporal Organization of the Striatum Encodes Action Space. Neuron 96, 949.

Koganezawa M, Kimura K-I, and Yamamoto D.(2016). The Neural Circuitry that Functions as a Switch for Courtship versus Aggression in *Drosophila* Males. Curr. Biol 26, 1395–1403. [PubMed: 27185554]

Kohatsu S, and Yamamoto D.(2015). Visually induced initiation of *Drosophila* innate courtship-like following pursuit is mediated by central excitatory state. Nat. Commun 6, 6457. [PubMed: 25743851]

Kohatsu S, Koganezawa M, and Yamamoto D.(2011a). Female Contact Activates Male-Specific Interneurons that Trigger Stereotypic Courtship Behavior in *Drosophila*. Neuron 69, 498–508. [PubMed: 21315260]

Kohatsu S, Koganezawa M, and Yamamoto D.(2011b). Female Contact Activates Male-Specific Interneurons that Trigger Stereotypic Courtship Behavior in *Drosophila*. Neuron 69, 498–508. [PubMed: 21315260]

Li Y, Zeng J, Zhang J, Yue C, Zhong W, Liu Z, Feng Q, and Luo M.(2018). Hypothalamic Circuits for Predation and Evasion. Neuron 97, 911–924.e5.

Markow TA, and Manning M.(1980). Mating success of photoreceptor mutants of *Drosophila melanogaster*. Behav. Neural Biol 29, 276–280. [PubMed: 6770840]

Martin JP, Guo P, Mu L, Harley CM, and Ritzmann RE (2015). Central-complex control of movement in the freely walking cockroach. Curr. Biol 25, 2795–2803. [PubMed: 26592340]

Mathis A, Mamidanna P, Cury KM, Abe T, Murthy VN, Mathis MW, and Bethge M.(2018). DeepLabCut: markerless pose estimation of user-defined body parts with deep learning. Nat. Neurosci 21, 1281–1289. [PubMed: 30127430]

McKinney RM, and Ben-Shahar Y.(2018) Visual recognition of the female body axis drives spatial elements of male courtship in Drosophila melanogaster. bioRxiv 10.1101/576322

Mendes CS, Bartos I, Akay T, Marka S, and Mann RS (2013). Quantification of gait parameters in freely walking wild type and sensory deprived Drosophila melanogaster. Elife 2, e00231.

Meissner GW, Dorman Z, Nern A, Forster K, Gibney T, Jeter J, Johnson L, He Y, Lee K, Melton B, et al. (2020). An image resource of subdivided Drosophila GAL4-driver expression patterns for neuron-level searches. bioRxiv 2020.05.29.080473.

Moore RJD, Taylor GJ, Paulk AC, Pearson T, van Swinderen B, and Srinivasan MV (2014). FicTrac: a visual method for tracking spherical motion and generating fictive animal paths. J. Neurosci. Methods 225, 106–119. [PubMed: 24491637]

Mueller JM, Ravbar P, Simpson JH, and Carlson JM (2019). *Drosophila melanogaster* grooming possesses syntax with distinct rules at different temporal scales. PLoS Comput. Biol 15, e1007105.

Namiki S, Dickinson MH, Wong AM, Korff W, and Card GM (2018). The functional organization of descending sensory-motor pathways in *Drosophila*. eLife 2018;7:e34272

Osumi-Sutherland D, Costa M, Court R, and O'Kane CJ (2014). Virtual Fly Brain - Using OWL to support the mapping and genetic dissection of the brain. CEUR Workshop Proc. 1265, 85–96. [PubMed: 29724079]

Otsuna H, Ito M, and Kawase T.(2018) Color depth MIP mask search: a new tool to expedite Split-GAL4 creation. bioRxiv 10.1101/318006

Pearson KG (1993). Common principles of motor control in vertebrates and invertebrates. Annu. Rev. Neurosci 16, 265–297. [PubMed: 8460894]

Pearson KG (1995). Reflex Reversal in the Walking Systems of Mammals and Arthropods. Neural Control of Movement 135–141.

von Philipsborn AC, Liu T, Yu JY, Masser C, Bidaye SS, and Dickson BJ (2011). Neuronal control of *Drosophila* courtship song. Neuron 69, 509–522. [PubMed: 21315261]

Piggott BJ, Liu J, Feng Z, Wescott SA, and Xu XZS (2011). The neural circuits and synaptic mechanisms underlying motor initiation in C. elegans. Cell 147, 922–933. [PubMed: 22078887]

Pnevmatikakis EA, and Giovannucci A.(2017). NoRMCorre: An online algorithm for piecewise rigid motion correction of calcium imaging data. J. Neurosci. Methods 291, 83–94. [PubMed: 28782629]

von Reyn CR, Nern A, Williamson WR, Breads P, Wu M, Namiki S, and Card GM (2017). Feature Integration Drives Probabilistic Behavior in the *Drosophila* Escape Response. Neuron 94, 1190–1204.e6.

Ren Q, Awasaki T, Huang YF, Liu Z, and Lee T.(2016). Cell Class-Lineage Analysis Reveals Sexually Dimorphic Lineage Compositions in the *Drosophila* Brain. Curr. Biol 26, 2583–2593. [PubMed: 27618265]

Rezával C, Pattnaik S, Pavlou HJ, Nojima T, Brüggemeier B, D'Souza LAD, Dweck HKM, and Goodwin SF (2016). Activation of Latent Courtship Circuitry in the Brain of *Drosophila* Females Induces Male-like Behaviors. Curr. Biol 26, 2508–2515. [PubMed: 27568592]

Ribeiro IMA, Drews M, Bahl A, Machacek C, Borst A, and Dickson BJ (2018). Visual Projection Neurons Mediating Directed Courtship in *Drosophila*. Cell 174, 607–621.e18.

Ruder L, and Arber S.(2019). Brainstem Circuits Controlling Action Diversification. Annu. Rev. Neurosci 42, 485–504. [PubMed: 31283898]

Ryckebusch S, and Laurent G.(1993). Rhythmic patterns evoked in locust leg motor neurons by the muscarinic agonist pilocarpine. Journal of Neurophysiology 69, 1583–1595. [PubMed: 8389831]

Seeds AM, Ravbar P, Chung P, Hampel S, Midgley FM Jr, , Mensh BD, and Simpson JH (2014). A suppression hierarchy among competing motor programs drives sequential grooming in *Drosophila*. eLife 3, e02951.

Seelig JD, and Jayaraman V.(2015). Neural dynamics for landmark orientation and angular path integration. Nature 521, 186–191. [PubMed: 25971509]

Seelig JD, Chiappe ME, Lott GK, Dutta A, Osborne JE, Reiser MB, and Jayaraman V.(2010). Two-photon calcium imaging from head-fixed *Drosophila* during optomotor walking behavior. Nat. Methods 7, 535–540. [PubMed: 20526346]

Sen R, Wu M, Branson K, Robie A, Rubin GM, and Dickson BJ (2017). Moonwalker Descending Neurons Mediate Visually Evoked Retreat in *Drosophila*. Curr. Biol 27, 766–771. [PubMed: 28238656]

Shik ML, and Orlovsky GN (1976). Neurophysiology of locomotor automatism. Physiol. Rev 56, 465–501. [PubMed: 778867]

Skinner RD, and Garcia-Rill E.(1984). The mesencephalic locomotor region (MLR) in the rat. Brain Res. 323, 385–389. [PubMed: 6525525]

Song J, Dahlberg E, and El Manira A.(2018). V2a interneuron diversity tailors spinal circuit organization to control the vigor of locomotor movements. Nat. Commun 9.3370 [PubMed: 30135498]

Staudacher EM (2001). Sensory responses of descending brain neurons in the walking cricket, Gryllus bimaculatus. J. Comp. Physiol. A 187, 1–17. [PubMed: 11318373]

Strausfeld NJ, and Bassemir UK (1983). Cobalt-coupled neurons of a giant fibre system in Diptera. J. Neurocytol 12, 971–991. [PubMed: 6420522]

Strausfeld NJ, and Gronenberg W.(1990). Descending neurons supplying the neck and flight motor of Diptera: organization and neuroanatomical relationships with visual pathways. J. Comp. Neurol 302, 954–972. [PubMed: 1707069]

Strauss R.(2002). The central complex and the genetic dissection of locomotor behaviour. Curr. Opin. Neurobiol 12, 633–638. [PubMed: 12490252]

Suver MP, Huda A, Iwasaki N, Safarik S, and Dickinson MH (2016). An Array of Descending Visual Interneurons Encoding Self-Motion in *Drosophila*. J. Neurosci 36, 11768–11780.

Talay M, Richman EB, Snell NJ, Hartmann GG, Fisher JD, Sorkac A, Santoyo JF, Chou-Freed C, Nair N, Johnson M, Szymanski JR, and Barnea G.(2017). Transsynaptic Mapping of Second-Order Taste Neurons in Flies by trans-Tango. Neuron 96, 783–795.e4.

Tirian L, and Dickson BJ (2017) The VT GAL4, LexA, and split-GAL4 driver line collections for targeted expression in the Drosophila nervous system. bioRxiv 10.1101/198648

Tóth TI, and Daun S.(2019). A kinematic model of stick-insect walking. Physiological Reports 7, e14080. [PubMed: 31033245]

Tóth TI, Knops S, and Daun-Gruhn S.(2012). A neuromechanical model explaining forward and backward stepping in the stick insect. J. Neurophysiol 107, 3267–3280. [PubMed: 22402652]

Tschida K, and Bhandawat V.(2015). Activity in descending dopaminergic neurons represents but is not required for leg movements in the fruit fly Drosophila. Physiol Rep 3.

Turner-Evans D, Wegener S, Rouault H, Franconville R, Wolff T, Seelig JD, Druckmann S, and Jayaraman V.(2017). Angular velocity integration in a fly heading circuit. eLife 2017;6:e23496

Tuthill JC, and Azim E.(2018). Proprioception. Curr. Biol 28, R194–R203. [PubMed: 29510103]

Wang Z, Singhvi A, Kong P, and Scott K.(2004). Taste Representations in the *Drosophila* Brain. Cell 117, 981–991. [PubMed: 15210117]

Weir PT, Henze MJ, Bleul C, Baumann-Klausener F, Labhart T, and Dickinson MH (2016). Anatomical Reconstruction and Functional Imaging Reveal an Ordered Array of Skylight Polarization Detectors in *Drosophila*. J. Neurosci 36, 5397–5404. [PubMed: 27170135]

Wosnitza A, Bockemuhl T, Dubbert M, Scholz H, and Buschges A.(2013). Inter-leg coordination in the control of walking speed in *Drosophila*. Journal of Experimental Biology 216, 480–491. [PubMed: 23038731]

Wu M, Nern A, Williamson WR, Morimoto MM, Reiser MB, Card GM, and Rubin GM (2016). Visual projection neurons in the lobula link feature detection to distinct behavioral programs. eLife 2016;5:e21022

Xu CS, Januszewski M, Lu Z, Takemura S, Hayworth KJ, Huang G, Shinomiya K, Maitin-Shepard J, Ackerman D, Berg S, et al. (2020). A Connectome of the Adult Drosophila Central Brain. bioRxiv 2020.01.21.911859.

Yu JY, Kanai MI, Demir E, Jefferis GSXE, and Dickson BJ (2010). Cellular organization of the neural circuit that drives *Drosophila* courtship behavior. Curr. Biol 20, 1602–1614. [PubMed: 20832315]

Zacarias R, Namiki S, Card GM, Vasconcelos ML, and Moita MA (2018). Speed dependent descending control of freezing behavior in *Drosophila melanogaster*. Nat. Commun 9, 3697. [PubMed: 30209268]

Zorovi M, and Hedwig B.(2013). Descending brain neurons in the cricket Gryllus bimaculatus (de Geer): auditory responses and impact on walking. J. Comp. Physiol. A Neuroethol. Sens. Neural Behav. Physiol 199, 25–34. [PubMed: 23104703]
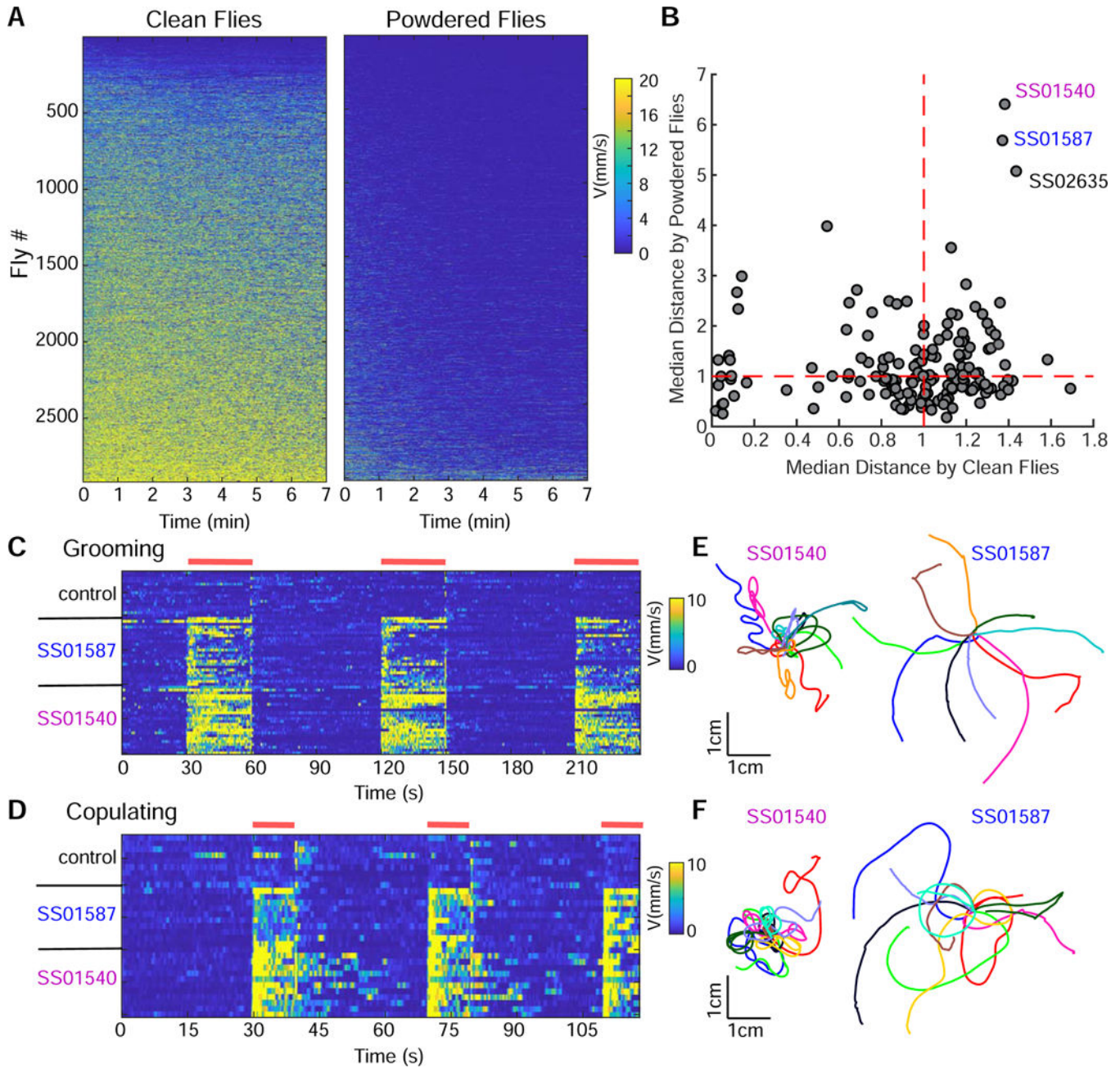
Highlights:

- Activating P9 or BPN initiates forward walking in stationary flies.

- P9 drives forward walking with ipsilateral turns whereas BPN drives straight walking.

- P9 receives inputs from LC9 and pC1 and contributes to mate pursuit.

- BPN is recruited during and required for fast, straight, long, forward walks.

Figure 1: Optogenetic screen identifies candidate walking initiation lines

(A) Translational velocity of non-powdered, "clean" flies (left) and "powdered", grooming flies (right) upon continuous optogenetic activation with CsChrimson throughout the 7 minute assay, shown as velocity heatmaps for individual flies arranged from lowest to highest mean velocity.

(B) Normalized median distance traveled by clean versus powdered flies for each genotype. n=12–16 per genotype per condition.

(C) Walking initiation upon transient activation in grooming flies for control, *SS01540* and *SS01587,* shown as velocity heatmaps for individual flies (red bars indicate light ON). n=16–24 flies/genotype.

(D) Walking initiation of females upon transient activation in copulating flies, shown as velocity heatmaps for individual flies (red bars indicate light ON). n=9–11 flies/genotype.

(E) Example walking trajectories, 4 seconds light ON, for *SS01540* and *SS01587* in the grooming assay, 10 flies/genotype.

(F) Example walking trajectories, 4 seconds light ON, for *SS01540* and *SS01587* in the copulation assay, 10 flies/genotype.

See Figure S1 for statistical analysis of candidate lines and Video S1, S2 for activation phenotypes.
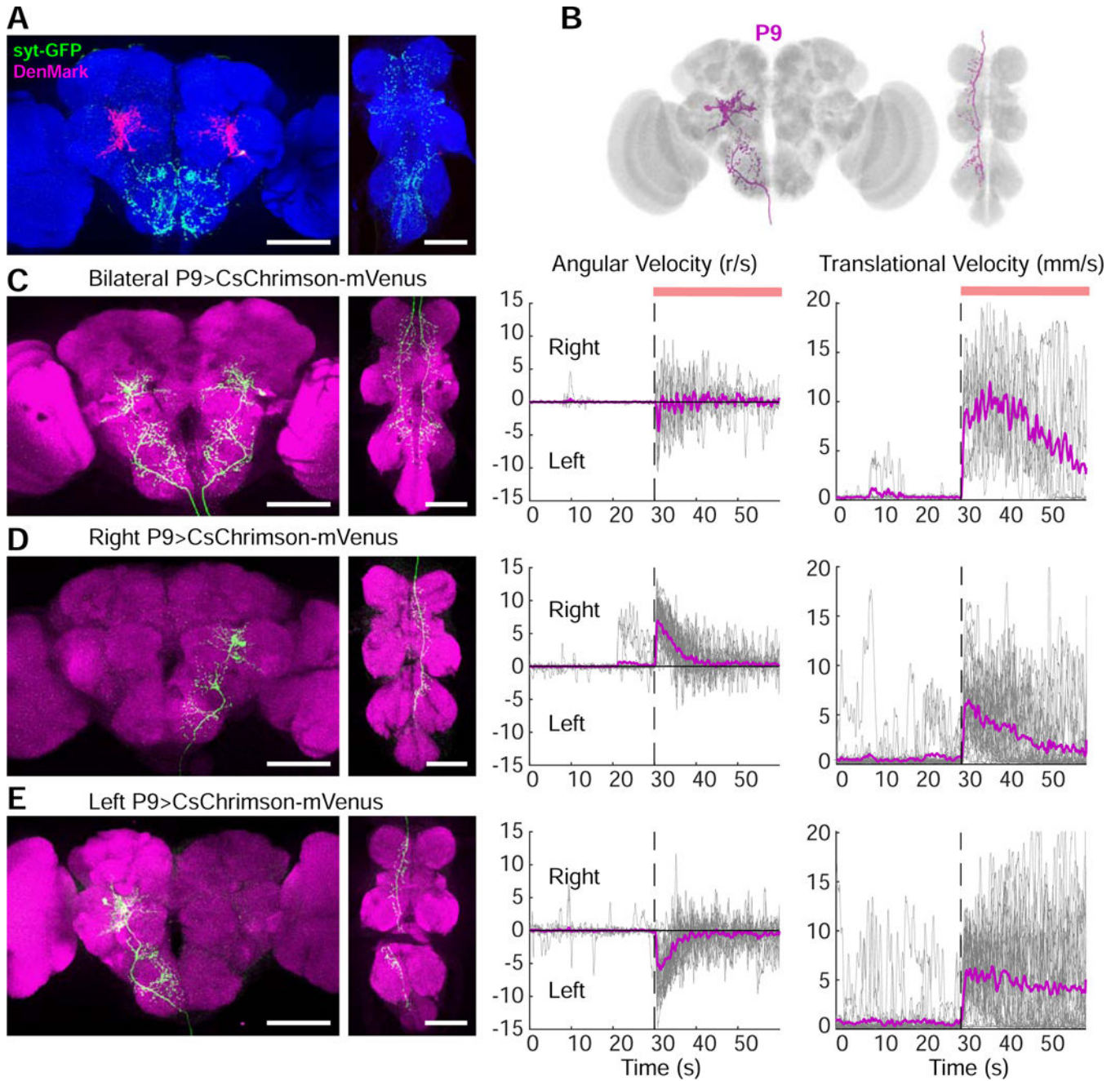
Figure 2: P9 activation triggers forward walking with ipsilateral turning
(A) DenMark (magenta) and synaptotagmin-GFP (green) in P9 neurites in the central brain (left) and VNC (right) of *SS01540>DenMark,Syt-GFP* flies. nc82 stains neuropil (blue). Scale 100 μm.
(B) P9 segmented image, mapped onto a fly brain template.
(C) CsChrimson-mVenus (green) and neuropil (magenta) (left), angular velocity with positive velocity for right turns, negative velocity for left turns (middle) and translational velocity (right) for mosaic animals with CsChrimson-mVenus in P9 neurons bilaterally (3 flies, 9 trials).

(D) CsChrimson-mVenus expression (left), angular velocity (middle) and translational velocity (right) for mosaic animals with CsChrimson-mVenus in right P9 neurons (10 flies, 30 trials).

(E) CsChrimson-mVenus expression (left), angular velocity (middle) and translational velocity (right) for mosaic animals with CsChrimson-mVenus in left P9 neurons (9 flies, 27 trials). Individual trials (grey), mean (magenta), light ON (red bar). See Figure S2 for characterization of an independent P9 split-Gal4 line. See Video S3 for activation phenotypes.
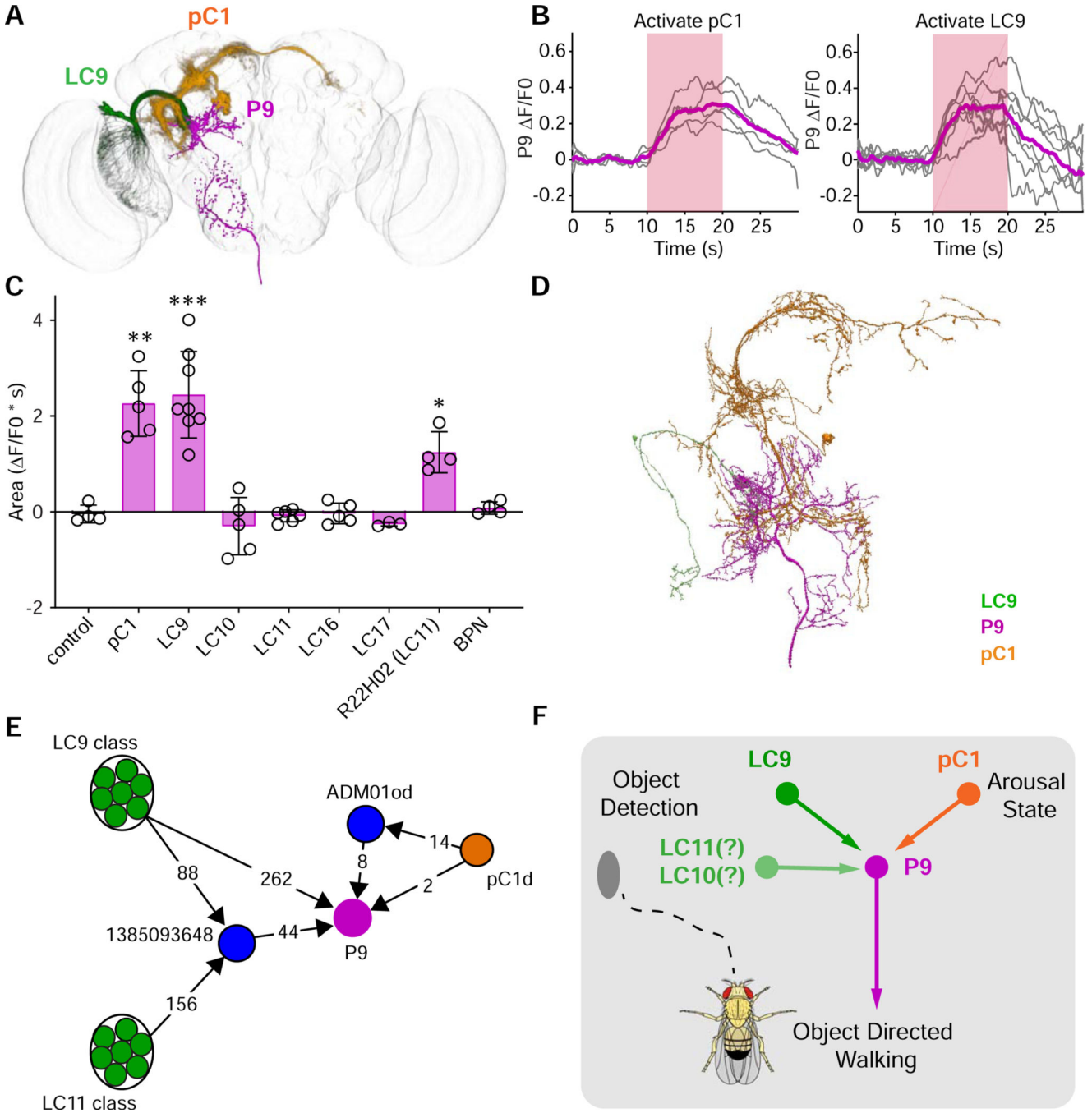
Figure 3: P9 neurons are activated by courtship promoting neurons and visual projection neurons.

(A) P9, pC1 and LC9 segmented neurons registered onto a template brain. See Figure S3 for anatomical overlap in single brains.

(B) GCaMP6s responses (AF/F) in P9 soma (using *P9-LexA, lexAop-GCaMP6s*) upon stimulation of pC1 (left) or LC9 (right), using *UAS-Chrimson88-tdTomato* and *R71G01-Gal4* for pC1 or LC9 split-Gal4. Trial averaged traces (grey), mean (magenta), optical stimulation (pink background). n=5–8 flies/genotype.

(C) P9 responses (area under average trial AF/F0 curve during light ON period) upon optical stimulation of candidate upstream neurons. n=3–8 per genotype, non-parametric Mann-Whitney test compared to no Chrimson control, *p<0.05, **p<0.01, ***p<0.001.

(D)EM reconstruction of the monosynaptically connected P9, pC1d and one LC9 cell

(E) Schematic summarizing EM connectivity analysis showing direct and indirect inputs on P9 by LC9 cluster (64 cells), pC1d (single cell) and LC11 cluster (58 cells), see Figure S3 for anatomy of intermediate neurons.

(F) P9 receives inputs from LC9 and pC1 and potentially from other VPNs like LC10, LC11, suggesting that it participates in object-directed tracking during courtship.
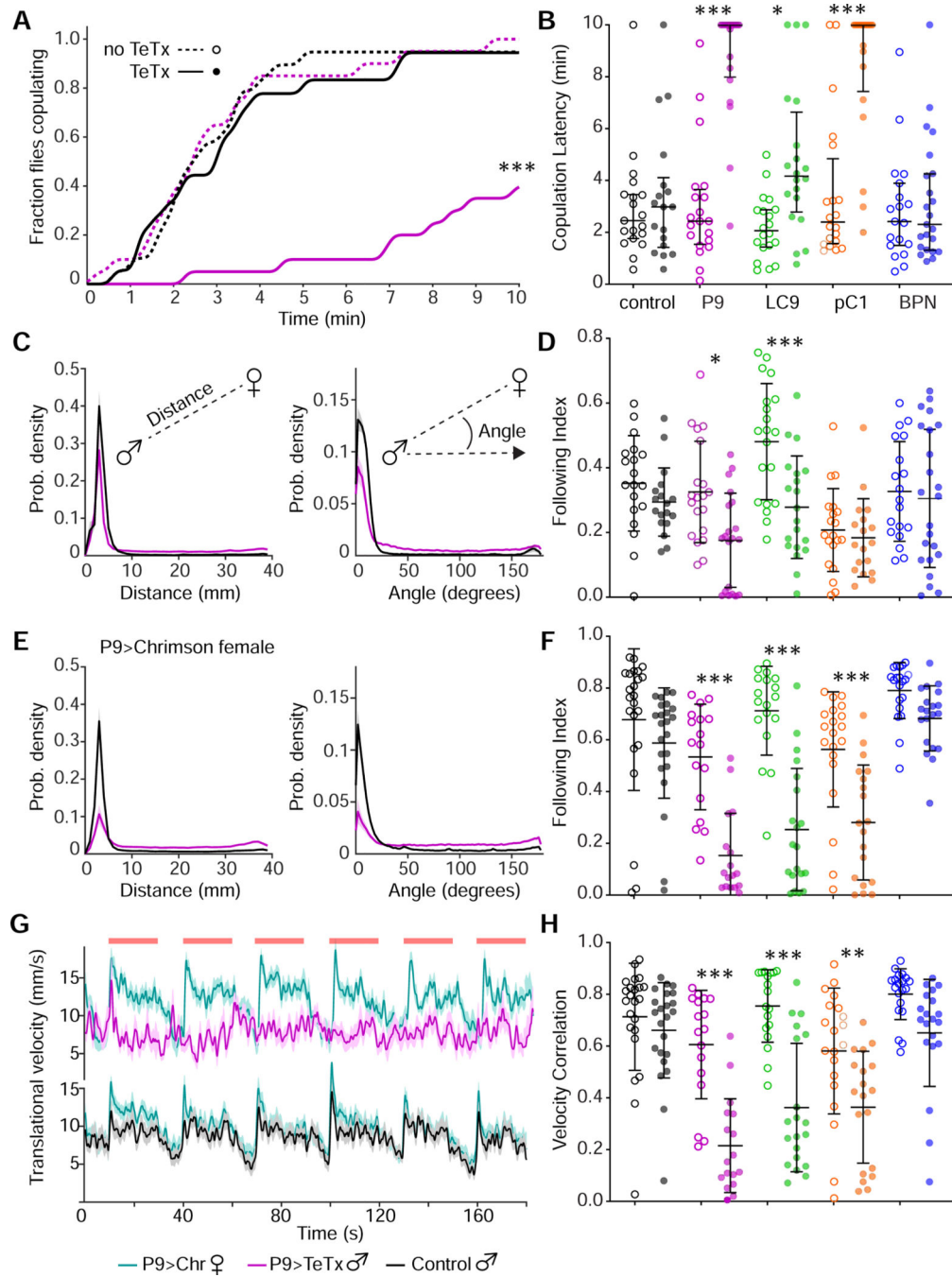
Figure 4: P9 is required for males to track females during courtship

(A) Fraction of males copulating with Canton S virgins over 10 minutes. *Gal4* controls (dotted lines; open circles for other panels), *Gal4*, *UAS-TeTx* flies (solid lines; filled circles for other panels), n=20–28 flies/genotype, Fisher's Exact Test, t = 10 min, ***p<0.001. Genotypes for all panels are color coded as B.

(B) Copulation latency. Lines indicate median and interquartile range. n=20–28 flies/genotype, Kruskal-Wallis test and Dunn's multiple comparison, *p<0.05, ***p<0.001.

(C) Probability density showing distance (left) or angle (right) between male and female, mean ± SEM.

(D) Following Index per courting pair. Lines indicate median and interquartile range. n=20–28 flies/genotype, ANOVA and Sidak's tests, *p<0.05, ***p<0.001.

(E) Probability density showing distance (left) or angle (right, 0° indicates female in front of male) between male and *P9>CsChrimson* "remote-controlled" female, mean ± SEM.

(F) Following Index per courting male and *P9>CsChrimson* female. n=17–23 flies/genotype, ANOVA and Sidak's tests, ***p<0.001.

(G) Translational velocity of *P9>TeTx* males and *P9>CsChrimson* females, or control males and *P9>CsChrimson* females, showing mean (dark) and SEM (shading), n = 17–23 pairs, red bar indicates light ON.

(H) Correlation between male and female velocities per courting pair, for males courting *P9>CsChrimson* females. n = 17–23 pairs, t-test with Sidak's multiple comparison corrections, **p<0.01, ***p<0.001.

See Figure S3 for additional characterization of P9 courtship phenotypes. See Figure S4 for gait analysis of *P9>TeTx* flies and Video S4 for courtship phenotype.

Figure 5: BPNs trigger forward walking with no turning bias

(A) *BPN-S1* split-Gal4 line, showing specific BPN expression (green), nc82 stains neuropil (magenta). Scale 100 μm

(B) Translational velocity of BPNS1 split-Gal4 (blue) or control (black) on activation with CsChrimson in grooming flies. n=8 flies, 24 trials, mean ± SEM.

(C) DenMark (magenta) and synaptotagmin (green) labeling in BPN-S1 line. nc82 stains neuropil (blue). Scale 100 μm.

(D) CsChrimson-mVenus (green) expression (left), angular velocity (middle) and translational velocity (right) for mosaic animals with CsChrimson-mVenus in BPNs bilaterally (4 flies, 12 trials).

(E) CsChrimson-mVenus expression (left), angular velocity (middle) and translational velocity (right) for mosaic animals with CsChrimson-mVenus in right BPNs (8 flies, 24 trials).

(F) CsChrimson-mVenus expression (left), angular velocity (middle) and translational velocity (right) for mosaic animals with CsChrimson-mVenus in left BPNs (8 flies, 24 trials).

Graphs in D-F show individual activation trials (grey), mean (blue), light ON (red bar). See Figure S5 for additional characterization of 2 BPN split-Gal4 lines.
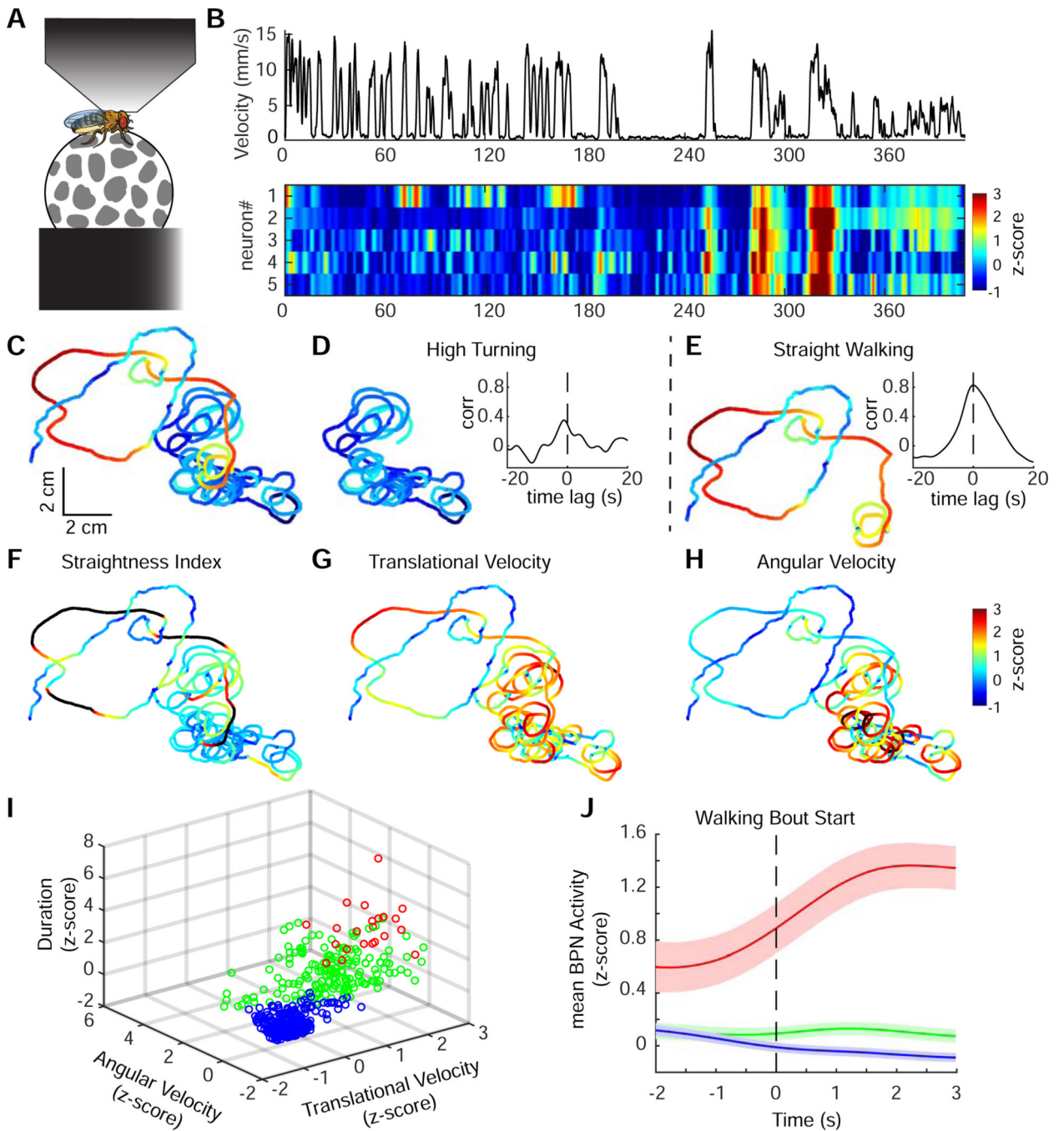
Figure 6: BPNs activity correlates with long, straight forward walks

(A) *in-vivo* imaging schematic of a fly walking on a ball.

(B) top: translational velocity of one fly during an imaging session, bottom: time-locked imaging readout of 5 BPN soma in the same fly, shown as z-scored GCaMP fluorescence.

(C-E) Trajectory of the fly in B color coded for mean BPN activity (z-score color-scale as B for the entire session (C), or first (D) or second half (E). Velocity versus mean BPN activity correlation plots for the first (D graph) and second half (E graph) of the imaging session.

(F-H) Trajectory of fly in B color coded with straightness index (F), translational velocity (G) and angular velocity (H).

(I) 3D subspace (velocity, angular velocity and walking duration.) representation of unbiased k-means clustering of 589 walking bouts across 3 flies and 5 imaging sessions.

(J) BPN activity (mean ± SEM) for each cluster aligned to walking bout start (dotted line). Cluster colors as in I. See Figure S6 for additional analysis of BPN activity.
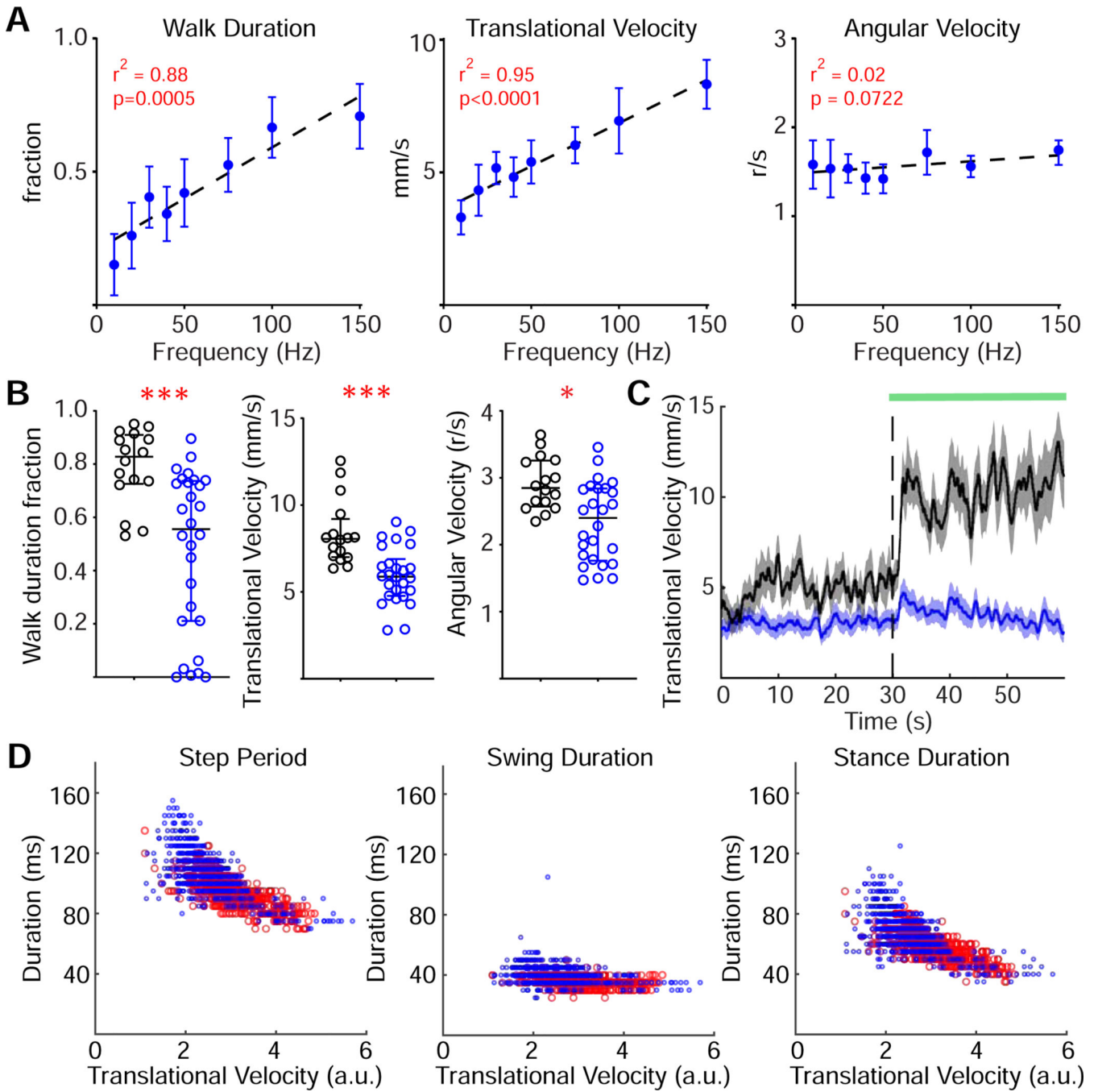
Figure 7: BPN activity levels reciprocally regulate straight, forward walking

(A) Walk duration (fraction of total activation time spent walking) (left), translational velocity (middle) and angular velocity (right) as a function of optogenetic activation (LED frequency) for *BPN>CsChrimson* flies. n=20 flies, mean ± 95%CI, linear regression line (dotted line) for r^2 values shown.

(B) Walk duration (left), translational velocity (middle) and angular velocity (right) of controls (black) and *BPN>TeTx* flies (blue). n= 16–28, Mann-Whitney, *p<0.05, ***p<0.001.

(C) Trial averaged translational velocity during green light stimulation for controls (black) and *BPN>TeTx* flies (blue). n=16–28, mean ± SEM, green bar indicates light ON.

(D) Middle leg step period (left), swing duration (middle) and stance duration (right) as a function of translational velocity of controls (red) and *BPN>TeTx* (blue), n=283–314 steps from 4–5 flies, t test. See Figure S7 for additional analysis of BPN silenced flies.

KEY RESOURCES TABLE

REAGENT or RESOURCE	SOURCE	IDENTIFIER
Antibodies		
anti-Bruchpilot (nc82, mouse monoclonal)	Developmental Studies Hybridoma Bank	RRID: AB_2314866
anti-GFP (chicken)	Thermo Fisher Scientific	RRID:AB_2534023
anti-GFP (rabbit)	Thermo Fisher Scientific	RRID:AB_221569
anti-RFP (rabbit)	CloneTech	RRID:AB_10013483
Goat anti-chicken, Alexa488	Thermo Fisher Scientific	RRID:AB_142924
Goat anti-rabbit, Alex488	Thermo Fisher Scientific	RRID:AB_2576217
Goat anti-rabbit, Alex568	Thermo Fisher Scientific	RRID:AB_10563566
Goat anti-mouse, Alex568	Thermo Fisher Scientific	RRID:AB_2534072
Goat anti-mouse, Alex647	Thermo Fisher Scientific	RRID:AB_141725
Chemicals, Peptides, and Recombinant Proteins		
Reactive Yellow 86 (CAS 61951–86-8)	Santan Cruz Biotechnology	Cat # sc-296260
All-trans retinal	Sigma-Aldrich	Cat # R2500
Experimental Models: Organisms/Strains		
Drosophila melanogaster: Canton S	N/A	N/A
Drosophila melanogaster : 20XUAS-IVS-CsChrimson.mVenus (attp18)	Bloomington Drosophila Stock Center	RRID:BDSC_55134
Drosophila melanogaster : w ^{1118} ;+;20XUAS-IVS-CsChrimson.mVenus (attp2)	Bloomington Drosophila Stock Center	RRID:BDSC_55136
Drosophila melanogaster : w+;UAS-TNT(E);+	Sweeney et al., 1995	N/A
Drosophila melanogaster : w, UAS-FRT-STOP-FRT-CsChrimson:Venus, hs-FLP2:PEST;+;+	Wu et al., 2016	N/A
Drosophila melanogaster: 10XUAS-syn21-Chrimson88-tdT3.1 attP18, LexAOP2-syn21-opGCaMP6s suHwattP8; +;+	Strother et al, 2017	N/A
Drosophila: w ^{1118} ;R38F04-LexA (attp40);+	Bloomington Drosophila Stock Center	RRID:BDSC_54708
Drosophila: w ^{1118} ;+;R71G01-Gal4 (attp2)	Bloomington Drosophila Stock Center	RRID:BDSC_39599
Drosophila: w ^{1118} ;+;R22H02-Gal4 (attp2)	Bloomington Drosophila Stock Center	RRID:BDSC_49304
Drosophila: w ^{1118} ;+;R11H10-Gal4 (attp2)	Bloomington Drosophila Stock Center	RRID:BDSC_48479
Drosophila: w ^{1118} ; VT023490-p65ADZp(attp40);R38F04-ZpGal4DBD(attp2)	Namiki et al, 2018	SS01540
Drosophila: w ^{1118} ; R11H10-p65ADZp;(attp40);VT033947-ZpGal4DBD(attp2)	Namiki et al, 2018	SS01587
Drosophila: w ^{1118} ; R42B02-p65ADZp;(attp40);VT037574-ZpGal4DBD(attp2)	Namiki et al, 2018	SS02635
Drosophila: w ^{1118} ; VT005105-p65ADZp(attp40);VT023490-ZpGal4DBD(attp2)	This study	N/A
Drosophila: w ^{1118} ; R11H10-p65.AD(attp40); VT025925-ZpGal4DBD(attp2)	This study	N/A

REAGENT or RESOURCE	SOURCE	IDENTIFIER
Drosophila: w ¹¹¹⁸; VT025925-p65.AD(attp40); R11H10-ZpGal4DBD(attp2)	This study	N/A
Drosophila: w ¹¹¹⁸; VT032961-p65.AD(attp40); VT027704-ZpGal4DBD(attp2)	Bloomington Drosophila Stock Center	RRID:BDSC_68245
Drosophila: w ¹¹¹⁸; R35D04-p65.AD; VT043656-ZpGal4DBD(attp2)	Bloomington Drosophila Stock Center	RRID:BDSC_68339
Drosophila: w ¹¹¹⁸; R22H02-p65.AD; R20G06-ZpGal4DBD(attp2)	Bloomington Drosophila Stock Center	RRID:BDSC_68362
Drosophila: w ¹¹¹⁸; 92B02-p65.AD (VK00027); R38E08-ZpGal4DBD(attp2)	Bloomington Drosophila Stock Center	RRID:BDSC_68376
Drosophila: w ¹¹¹⁸; +;R21D03-Gal4	Bloomington Drosophila Stock Center	RRID:BDSC_49860
Drosophila: w ¹¹¹⁸; UAS-DenMark, UAS-syt.eGFP; In(3L)D, mirr ^{SaiD1} D ¹ /TM6C, Sb ¹	Bloomington Drosophila Stock Center	RRID:BDSC_33064
Drosophila: w ¹¹¹⁸; UAS-DenMark, L ¹ /CyO; UAS-DenMark, UAS-syt.eGFP	Bloomington Drosophila Stock Center	RRID:BDSC_33065
Drosophila: yw,UAS-myrGFP,QUAS-mtdTomato (attp8);trans-Tango (attp40)	Talay et al, 2017	N/A
Software and Algorithms		
FicTrac	Moore et al., 2014	http://rjdmoore.net/fictrac/
DeepLabCut	Mathis et al, 2018	https://github.com/AlexEMG/DeepLabCut
VV3D	Otsuna et al.	https://github.com/takashi310/VVD_Viewer
FlyTracker-1.0.3	Eyjolfsdottir et al., 2014	http://www.vision.caltech.edu/Tools/FlyTracker/download.html
CalmAn-MATLAB	Giovannucci et al., 2019	https://github.com/flatironinstitute/CaImAn-MATLAB
NormCorre	Pnevmatikakis and Giovannucci, 2017	https://github.com/flatironinstitute/NoRMCorre
Other		